AGU PUBLICATIONS

JGR

Journal of Geophysical Research: Oceans

RESEARCH ARTICLE

10.1002/2016JC012175

Temperature flux carried by individual eddies across 47°N in the Atlantic Ocean

Vasco Müller[1,2], Dagmar Kieke[1,2], Paul G. Myers[3], Clark Pennelly[3], and Christian Mertens[2]

[1]MARUM - Center for Marine Environmental Sciences, University of Bremen, Bremen, Germany, [2]Institute of Environmental Physics, University of Bremen, Bremen, Germany, [3]Department of Earth and Atmospheric Sciences, University of Alberta, Edmonton, Alberta, Canada

Key Points:
- Eddies identified in the North Atlantic are combined with SST anomalies to quantify temperature fluxes across 47°N
- Individual strong eddies related to extreme temperature anomalies carry ~25% of the temperature fluxes
- Key findings are consistent between observations and two model simulations with different resolution

Correspondence to:
V. Müller,
vasco.mueller@uni-bremen.de

Citation:
Müller, V., D. Kieke, P. G. Myers, C. Pennelly, and C. Mertens (2017), Temperature flux carried by individual eddies across 47°N in the Atlantic Ocean, *J. Geophys. Res. Oceans*, *122*, 2441–2464, doi:10.1002/2016JC012175.

Received 22 JUL 2016
Accepted 27 FEB 2017
Accepted article online 2 MAR 2017
Published online 24 MAR 2017

Abstract Surface geostrophic velocity fields derived from satellite altimetry between January 1993 and April 2014 are used to detect and investigate eddies in the North Atlantic between 40°N–55°N and 60°W–10°W. Focus is on a zonal section along 47°N, roughly at the boundary between the subpolar and the subtropical gyres. Sea surface temperature data are used to quantify the temperature anomalies associated with eddies and the respective surface temperature fluxes related to these eddies. Identified eddy pathways across 47°N are related to the mean background velocity from full-depth ship observations carried out on 11 cruises between 2003 and 2014. The analysis is repeated in two model simulations with 1/4° and 1/12° horizontal resolution, respectively, for the period 2002–2013. The analysis reveals almost 37,000 altimeter-derived eddies with a lifetime longer than 1 week in the area. The highest number of eddies is found along the pathway of the North Atlantic Current, roughly following the 4000 m isobath, and on the Grand Banks of Newfoundland. Time series of temperature fluxes by eddies crossing 47°N reveal that single isolated eddies with large SST signatures contribute ~25% to the surface temperature flux. Relating the observed eddies to the observed top-to-bottom velocity distribution at 47°N points to the existence of eddy pathways across 47°. The highest-temperature fluxes are linked to the fastest and most pronounced current branches in the western Newfoundland Basin. While there are fewer eddies in both model simulations, the key findings are consistent between the observations and the two model simulations.

1. Introduction

The North Atlantic between 40°N–55°N is influenced by two vastly different regimes of currents and water masses: the subpolar gyre, a large-scale cyclonic circulation cell, and the anticyclonic circulation cell of the subtropical gyre. A well-defined meridional front, located off the shallow Grand Banks of Newfoundland that, to the east, widens and runs zonally, separates the warm subtropical gyre and the cold subpolar gyre. It is prominent in the spatial distribution of the mean sea surface temperature (SST) as well as the mean geostrophic velocities (Figure 1a).

In the Newfoundland Basin, the Western Boundary Current (WBC) and the North Atlantic Current (NAC) flow in different directions along the boundary of the two gyres. The deep reaching WBC originating in the north transports cold and fresh (subpolar) water southward, i.e., from the deep water formation regions along the western continental margin toward lower latitudes (Figure 1a). Here we will use the term WBC not only for the bottom-intensified part of the deep southward flow but for the total southward flow along the continental margin.

The NAC, on the other hand, transports warm, saline (subtropical) surface and subsurface waters as the continuation of the Gulf Stream [e.g., *Rossby*, 1996], as well as recirculating subpolar gyre water from the boundary current in deeper layers [*Mertens et al.*, 2014]. Southeast of the Grand Banks of Newfoundland, the NAC flows in a northeastward direction, forming a permanent anticyclonic feature centered around 42°N and 44°W (the so-called Mann-Eddy) [*Mann*, 1967; *Rossby*, 1996]. The NAC then follows the topography northward roughly along the 4000 m isobath and forms several recirculation cells in the Newfoundland Basin [*Rossby*, 1996; *Kearns and Rossby*, 1998; *Mertens et al.*, 2014]. At the so-called Northwest Corner, an anticyclonic feature located at around 52°N, the NAC turns eastward. The NAC then crosses the Mid-Atlantic Ridge (MAR), often splitting into different branches and alternating between different

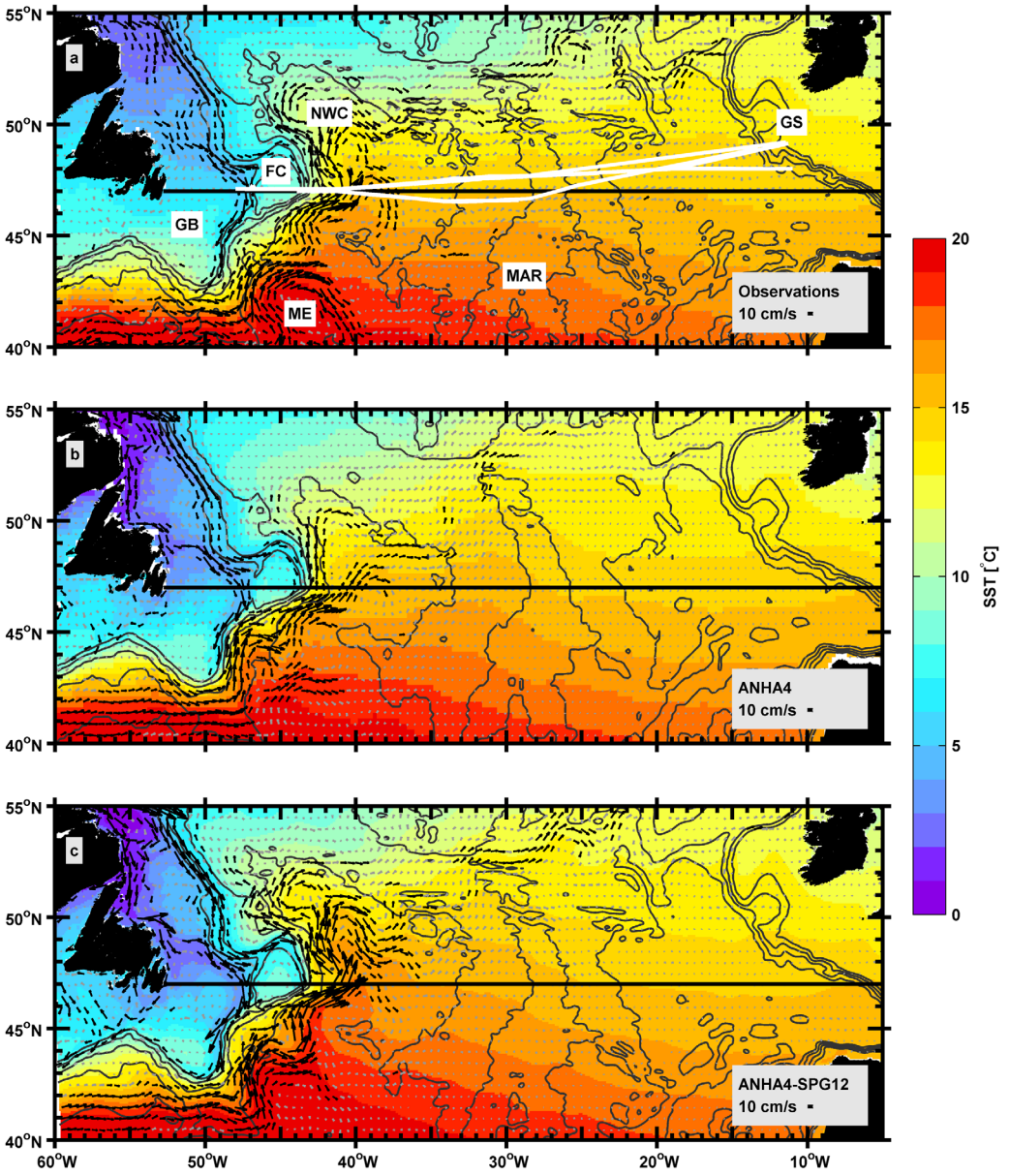

Figure 1. Mean geostrophic velocities and mean SST in the study region for the period January 2002 to December 2013. The locations of prominent topographic and circulation features are shown in the top figure (ME: Mann Eddy, GB: Grand Banks, FC: Flemish Cap, NWC: North West Corner, GS: Goban Spur, MAR: Mid-Atlantic Ridge). (a) Mean AVISO geostrophic velocities from absolute dynamic topography (DT-MADT) and mean NOAA Optimum Interpolation SST V2 are shown for the observations. For the model simulations ((b) 1/4° ANHA4 simulation and (c) 1/12° ANHA4-SPG12 simulation), the mean geostrophic velocities and mean SST from the respective model runs are shown. Mean velocities exceeding 10 cm s^{-1} are indicated with black arrows. Only every second velocity vector is plotted for the observations and the ANHA4 simulation and every sixth vector for the ANHA4-SPG12 simulation. The white lines in Figure 1a indicate the tracks of the 11 cruises conducted along nominally 47°N between 2003 and 2014. The black line indicates the section at 47°N. Isobaths are given every 1000 m using bathymetry derived from the ETOPO1 data set [*Amante and Eakins*, 2009] for the observations and the respective model bathymetry of the model simulations. The bathymetries in Figures 1a and 1c are low-pass-filtered to highlight general features.

pathways close to or through the fracture zones located between 48°N and 53°N [*Schott et al.*, 1999; *Bower and von Appen*, 2008].

On its way along the western continental margin, the Gulf Stream/NAC has to cross several topographic obstacles (e.g., New England-, Corner Rise-, and Newfoundland Seamounts) where it experiences disruptions, forms meanders, and sheds individual eddies [e.g., *Rossby*, 1996]. This leads to regions of increased eddy kinetic energy (EKE) along the pathway of the NAC and in the Newfoundland Basin (Figure 3a) [e.g., *Rossby*, 1996; *Carr and Rossby*, 2001].

There is significant exchange between the boundary and the interior of the North Atlantic by subpolar water detaching from the WBC, as observed by *Bower et al*. [2009] and *Kieke et al*. [2009]. This exchange was quantified by *Mertens et al*. [2014]. The southward flow of the WBC transports about 30 Sv of deep water ($\sigma_\Theta > 27.68$ kg m^{-3}) toward 47°N, with about 15 Sv leaving the WBC, recirculating northward between 42°N and 47°N and thus contributing to the deep NAC [*Mertens et al*., 2014].

All of the above mentioned studies have shown that the region between 45°N and 50°N in the western subpolar North Atlantic is a highly dynamic region. In this region eddies and other mesoscale features are of great relevance for the local exchange and horizontal mixing and stirring of water masses from different origin and of different properties [e.g., *Robinson*, 1983; *Abraham and Bowen*, 2002; *Waugh and Abraham*, 2008]. However, quantified knowledge on the role of individual eddies for this horizontal exchange is still limited, and their respective contribution needs to be investigated.

For most of the world's ocean, the kinetic energy of mesoscale features is larger than the kinetic energy of the mean flow. More importantly for this study, individual eddies can carry water from their respective source region inside their cores and entrain surrounding water into their outer ring. The properties of these waters (e.g., temperature, salinity, oxygen, or nutrients) are then transported with the eddy over longer distances and released gradually by dissipation and mixing or more abruptly when the eddy decays [e.g., *Robinson*, 1983]. This effect provides an important mechanism of cross-frontal transport between the subpolar and subtropical gyres of the North Atlantic [*Dutkiewicz et al*., 2001] and between the subpolar water from the WBC and the open ocean in the Newfoundland Basin [*Bower et al*., 2011]. Using the 1/12° resolution FLAME model, *Rhein et al*. [2011] found that ~60% of the modeled heat flux variability at 47°N is caused by the turbulent (i.e., high frequency) component of the velocity field, but so far the role of individual eddies (i.e., coherent vortices) for this variability remains unclear.

With the introduction of high-resolution, eddy resolving models (see review by *Hecht and Hasumi* [2008]), as well as satellite altimetry and automated eddy detection schemes [e.g., *Chelton et al*., 2007, 2011; *Nencioli et al*., 2010], it has become increasingly common to assess the role of individual eddies rather than the eddy (i.e., turbulent) component of the velocity field. For example, *Dong et al*. [2014] and *Zhang et al*. [2014] have demonstrated that by direct identification and tracking of single eddies and the integration of the tracer anomalies within the eddies, they can follow the anomalies along the eddy's trajectory and calculate fluxes by individual eddies.

The present study aims to contribute to a better understanding of the role of individual eddies for the spatial exchange of waters in the region of the boundary of the subpolar and subtropical gyres in the North Atlantic. We center our analysis on surface temperature fluxes of individually detected eddies, derived from satellite altimetry and sea surface temperature (SST) observations. Both data sets have the advantage of high temporal and spatial coverage and thus provide a long-term time series spanning over more than two decades (1993–2014) at a high temporal and spatial resolution (1 day and 1/4°). Focus is on the meridional flux of anomalously cold or warm surface water trapped within eddies as they cross 47°N. There we can relate the satellite-derived temperature fluxes of individual eddies inferred at the surface to the top-to-bottom velocity structure inferred from repeated shipboard velocity measurements along this latitude in the period 2003–2014 [*Rhein et al*., 2011; *Mertens et al*., 2014].

The analysis is subsequently applied to the output from two NEMO (Nucleus for European Modelling of the Ocean [*Madec and the NEMO team*, 2008]) model simulations with different horizontal resolution: (1) Arctic Northern Hemisphere Atlantic configuration with 1/4° horizontal resolution (ANHA4) and (2) ANHA4 with a nested 1/12° horizontal resolution encompassing the subpolar North Atlantic, called ANHA4-SPG12. The ANHA4 setup has the same horizontal resolution as the altimeter-derived velocity observations, and the ANHA4-SPG12 setup represents finer resolution allowing us to assess the impact of different spatial resolution on the results. If the model compares well to the observed temperature flux by individual eddies across 47°N, it can be used in future studies to extend the analysis to regions where we have little to no observational data.

The following questions will be investigated in this study:

1. What is the spatial distribution of detected eddies in the southern subpolar North Atlantic, and what are their properties?

2. What is the surface temperature flux carried by eddies across 47°N?
3. Is there a notable contribution of certain eddies to the temperature flux carried by all eddies across 47°N?
4. Are there main eddy pathways, and can they be connected to the major circulation branches in this region?
5. How well are the temperature fluxes and spatial patterns of individual eddies simulated in the two versions of the NEMO model?
6. Is there an impact of the different horizontal resolution in the two NEMO configurations on the simulated results?

The structure of the paper is as follows: in section 2, we describe the observational data, the model configuration, and the technique used to detect eddies. We then compare the characteristics of the detected eddies between observations and model (section 3). We analyze the surface temperature fluxes of eddies crossing 47°N (section 4) and relate the respective pathways of the eddies to the meridional velocity distribution at this latitude (section 5). Section 6 provides a discussion of the results, the conclusions, and an outlook.

2. Data and Methods

2.1. Velocity Fields From Satellite Altimetry Data

To identify surface signatures of eddies, we use geostrophic velocity fields derived from a mapped sea level anomaly data set, specifically the "all-sat-merged" delayed time DT-MSLA product, version 15.0, provided by AVISO (http://www.aviso.altimetry.fr/duacs/). The sea level anomaly (SLA) observations stem from the SSALTO/Duacs multimission altimeter product [*Le Traon et al*., 1998; *Ducet et al*., 2000], a combined product from different satellite altimetry missions. Using the altimetry data from multiple platforms reduces the error of the SLA, while improving the spatial resolution [*Le Traon et al*., 2003]. The considered SLA fields are mapped on a 1/4° × 1/4° Mercator grid, have a daily resolution, and are available at the time of writing for the period January 1993 to April 2014. The daily resolution is a product of the processing of the data and cannot be achieved directly by satellite coverage. The corresponding near-real time product has been used in Figure 10. It is available for a longer period and contains more recent data but is lower in quality than the delayed time data [*SSALTO/Duacs*, 2014]. The anomalies in the data set are calculated with respect to the 20 year mean for the years 1993–2012 [*SSALTO/Duacs*, 2014]. Velocity anomalies (u,v) are then derived from each SLA map assuming geostrophic balance

$$u = -\frac{g}{f}\frac{\partial SLA}{\partial y}, v = \frac{g}{f}\frac{\partial SLA}{\partial x}, \tag{1}$$

where g is the gravitational acceleration, f is the Coriolis parameter, and $\frac{\partial SLA}{\partial x}$ $\left(\frac{\partial SLA}{\partial y}\right)$ is the gradient of the sea level anomaly in zonal (meridional) direction. For the purpose of eddy detection, we are interested in intraseasonal changes of the velocity field. Hence, we calculate the mean annual cycle for each velocity component at every grid point and subtract it from the original velocity field. Analysis is focused on the North Atlantic ranging from 60°W–10°W and 40°N–55°N. For inferring the mean velocity field shown in Figure 1, we used the absolute geostrophic velocities from absolute dynamic topography (DT-MADT, sum of SLA and mean dynamic topography), since averaging over the SLA would result to zero.

2.2. ANHA4 and ANHA4-SPG12 Configurations of the NEMO Model

The model simulations analyzed in this study were carried out with the Nucleus for European Modeling of the Ocean (NEMO) model numerical framework version 3.4 [*Madec and the NEMO team*, 2008]. The ocean model includes the 3-D, linear free surface, hydrostatic, primitive-equations coupled to the Louvain-la-Neuve sea-ice model (LIM2) [*Fichefet and Morales Maqueda*, 1997]. The ocean model consists of 50 vertical levels with 1 m thickness for the top layer and decreasing vertical resolution with depth. The sea ice module has an elastic-viscous-plastic (EVP) ice rheology [*Hunke and Dukowicz*, 1997] with no-slip lateral boundary conditions for the sea ice and free-slip lateral boundary conditions for the ocean. Two different model configurations have been considered in this study.

The Arctic Northern Hemisphere Atlantic configuration with 1/4° horizontal resolution (ANHA4) is a subdomain of the global tripolar ORCA025 configuration [*Barnier et al*., 2007]. A map of the model domain with

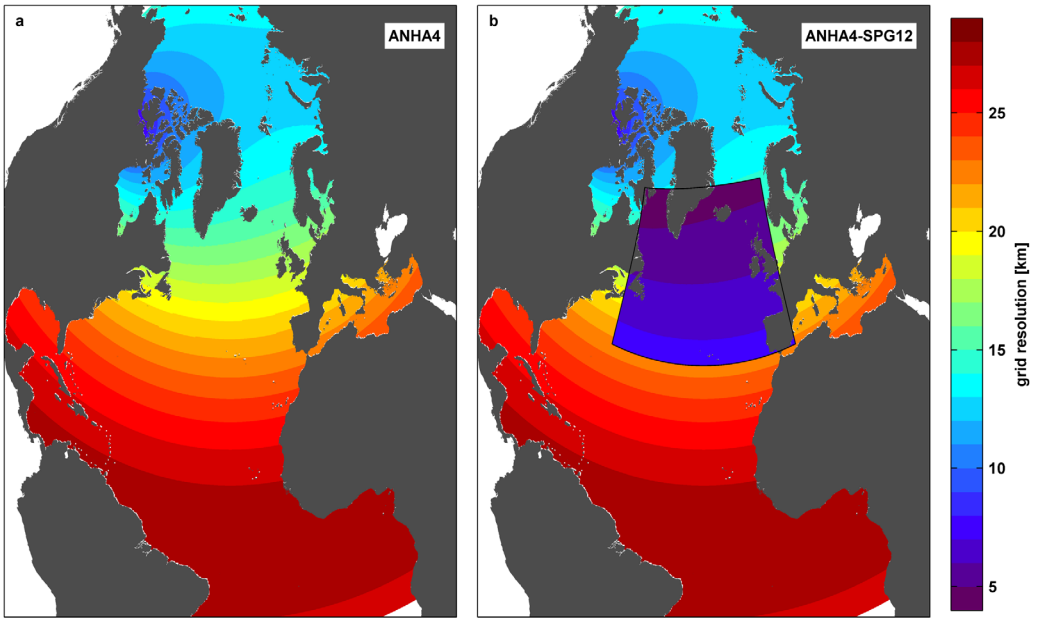

Figure 2. (a) Horizontal grid resolution of the ANHA4 model domain and the (b) two-way nested ANHA4-SPG12 subdomain in the subpolar gyre region. ANHA4 is a subdomain of the global ORCA025 mesh [*Barnier et al*., 2007].

the respective horizontal grid resolution is shown in Figure 2a. This regional configuration has been used in the past for studying the circulation and deep convection in the Labrador Sea [*Holdsworth and Myers*, 2015] and the spreading of Greenland freshwater in the subarctic seas [*Dukhovskoy et al*., 2016]. The model domain of this configuration covers the whole North Atlantic and the Nordic Sea (including the Gulf of Mexico in the west and the Mediterranean Sea in the east) with open boundaries at 20°S and the Bering Strait. The open boundary conditions are provided from the Global Ocean Reanalyses and Simulations (GLORYS2v3) reanalysis from MERCATOR [*Ferry et al*., 2010]. The initial conditions for the model simulation stem from the same reanalysis product.

The model is forced with atmospheric data from the Canadian Meteorological Centre's Global Deterministic Prediction System (CGRF) [*Smith et al*., 2014], with 1 h temporal resolution, and a horizontal resolution of 0.45° longitude and 0.3° latitude. Runoff forcing is obtained from the monthly runoff climatology by *Dai et al*. [2009], manually remapped to the model grid to preserve runoff and watershed volumes (X. Hu, personal communication, 2015). No relaxation is applied to the model salinity during the simulation. The time step of the ANHA4 configuration is 1080 s, and the output is saved every 5 days for the period January 2002 to December 2013.

The second model configuration (ANHA4-SPG12) consists of a subregion with 1/12° horizontal resolution two-way nested in the ANHA4 configuration using the Adaptive Grid Refinement In Fortran (AGRIF) tool [*Debreu et al*., 2008]. The inner high-resolution nest covers the subpolar gyre region between 36°N and 70°N, with a zonal extent from 0°W to 60°W south of Newfoundland and around 70°W in the northern Labrador Sea (Figure 2b). Apart from resolution-dependent parameters (e.g., the model time step, horizontal and vertical viscosity) all parameters as well as the vertical resolution are kept identical to the ANHA4 configuration. The time step for the ANHA4-SPG12 simulation is 180 s, and the output is also saved every 5 days for the period January 2002 to December 2013.

Vertical mixing at subgrid scales in both configurations is parameterized using a turbulent kinetic energy (TKE) closure model [*Madec and the NEMO team*, 2008]. For lateral mixing the model uses a bi-Laplacian operator with an eddy viscosity of 1.5×10^{11} m^4/s for the ANHA4 configuration and 1.0×10^{10} m^4/s for the ANHA4-SPG12 configuration. Subgridscale tracer lateral diffusion is parameterized with an isopycnal Laplacian operator with a horizontal eddy diffusivity of 300 m^2/s for the ANAH4 configuration and 50 m^2/s for the ANHA4-SPG12 configuration.

Our study region (40°N–55°N) is located in the center of the model domain, so no spurious effects from the boundaries of the nesting region (ANHA4-SPG12) or from the open boundary conditions of the ANHA4 domain are expected. The sea level anomalies of the respective model simulations are linearly interpolated from the curvilinear model grid to a regular longitude/latitude grid. The geostrophic velocities were then calculated exactly the same way as the altimeter-derived velocities using equation (1).

While the mean circulation is generally weaker and smoother in the ANHA4 simulation than in the observations and the ANHA4-SPG12 simulation, the patterns of the mean circulation in both model simulations correspond well to the observed mean absolute geostrophic velocities detected from satellite altimetry (Figure 1). In both simulations as in the observations, there are clearly defined northward and southward boundary currents, the Mann-Eddy, several recirculation cells in the Newfoundland Basin, as well as the Northwest Corner and the pathway over the fracture zones of the MAR. Only the coastal branch of the Labrador Current is more pronounced in the models than in the observations.

2.3. Automatic Detection of Individual Eddies

Assessing the role of eddies for the temperature flux across 47°N requires an adequate automatic eddy detection technique. Automatic detection and tracking of eddies in the ocean has been (and still is) far from being a trivial task, and there are many studies making use of different methods of eddy detection. This was done for example by analyzing the Okubo-Weiss parameter (the ratio between strain/shear and relative vorticity [*Okubo*, 1970; *Weiss*, 1991; *Isern-Fontanet et al*., 2003; *Chelton et al*., 2007, 2011]), by wavelet analysis of the relative vorticity [e.g., *Doglioli et al*., 2007], closed contours of SLA [e.g., *Faghmous et al*., 2015], or by direct analysis of the flow geometry [e.g., *Nencioli et al*., 2010]. None of these detection methods is perfect, and every method has its strengths and weaknesses.

For the study region in the North Atlantic, we choose the vector geometry-based algorithm following *Nencioli et al*. [2010] for both the observations and the model simulations. A full description of the algorithm is given by *Nencioli et al*. [2010], but the major steps are summarized below. The algorithm consists of three steps: (1) detecting eddy centers, (2) identifying the eddy boundary, and (3) tracking the eddy.

Step 1: For the detection of possible eddy centers, every daily snapshot of the velocity field is analyzed using four constraints:

1. The meridional velocity v has to reverse sign and increase radially with distance from the center along a zonal section with the distance of "a" grid points around the potential eddy center.
2. For the points matching constraint (1), the zonal velocity u has to reverse sign and increase radially within a meridional section of the same length "a" around the center. The sense of rotation for u has to be the same as for v.
3. The potential eddy center has to be the local minimum of velocity within a box with edge length of "b" grid points around the center.
4. In order to avoid false identification of meanders and divergent zones as eddies, the velocity vectors have to rotate gradually in the same direction within a box of "$a - 1$" grid points around the potential center of the eddy. This makes the algorithm ideal for the study region, which is characterized not only by eddies but also by strong meandering of the NAC.

Points on the grid that satisfy all four constraints are then defined as eddy centers. The algorithm requires the parameters a and b to be chosen with respect to the horizontal resolution of the velocity field. *Liu et al*. [2012] found the ideal set of parameters for the AVISO velocity field to be $a = 3$ grid points, and $b = 2$ grid points. These values are used here as well. Following *Liu et al*. [2012], the velocity fields from the observations and the ANHA4 simulation are linearly interpolated from 1/4° × 1/4° to 1/6° × 1/6° resolution before applying the algorithm. This does not change any features in the velocity field while improving the algorithm's performance. For the ANHA4-SPG12 simulation with 1/12° × 1/12° horizontal resolution we found $a = 5$ grid points and $b = 3$ grid points to be the setting with the highest detection rate. This was tested by repeatedly running the algorithm with different sets of parameters for a subregion in the NAC that includes eddies as well as meanders and comparing the success of eddy detection by visual inspection.

Step 2: The velocity field around each detected eddy center is integrated and the local stream function calculated. Following *Nencioli et al*. [2010], the eddy boundary is then defined as the largest closed contour of the local stream function around the eddy center. We define the eddy radius (R) as the mean distance of all

grid points of the eddy boundary to the eddy center. Our analysis excludes very small features by not taking into account any eddies with a radius smaller than $R_{min}=20\times cos(\phi)$ km, where ϕ is the latitude of the eddy center (i.e., eddies with a radius that is only represented by one grid cell of the interpolated grid or two grid cells of the ANHA4-SPG12 grid are not taken into account).

Step 3: Last, the detected eddies are tracked through time to determine the eddies' trajectories. The eddy tracking method used here is in principal very similar to most automated eddy tracking procedures [e.g., *Isern-Fontanet et al*., 2003; *Doglioli et al*., 2007; *Chelton et al*., 2007, 2011; *Chaigneau et al*., 2008]. An eddy track between successive time steps is defined when an eddy of the same rotation (cyclone/anticyclone) can be found at time step t_{n+1} within a defined search radius around the initial centers position at time step t_n. In case no successive eddy can be detected at t_{n+1}, the next time step t_{n+2} is analyzed. If no continuous eddy track can be found for two successive time steps, the eddy is regarded as dissolved.

The reliability of eddy tracking depends on the definition of the search radius. This in turn depends on the temporal and spatial resolution of the data, as well as on the phase speed of long baroclinic Rossby waves at the location of the respective eddy [*Chelton et al*., 2007, 2011]. Since the eddy translation speed is not known a priori of running the algorithm, we use a typical phase speed of baroclinic Rossby waves in the study region (20 cm s^{-1} [*Chelton et al*., 1998]). Following *Chelton et al*. [2011], the search radius should be 1.75 times the distance that a long baroclinic Rossby wave would propagate. This leads to a search radius of 30 km for the observations with daily resolution. Using the same assumption in the 5 day resolution of the model output would suggest a search radius of about 150 km. In practice, 150 km led in almost all cases to ambiguous eddy tracks, and therefore a smaller search radius of only 40 km was chosen as the most appropriate for the model simulations. In order to improve the eddy tracking, the detected tracks are postprocessed as suggested by *Faghmous et al*. [2015], by merging terminated trajectories with new trajectories starting in the neighborhood of the termination point. Nevertheless, some splitting of eddy tracks (in observations and model) cannot be avoided. After the postprocessing step, very short lived eddies with a life time of less than 7 days are removed and not considered for further analysis. For the model simulations this means that an eddy has to exist for at least two steps of the saved output (i.e., 10 days). The eddy translation speed is then calculated simply as the distance of displacement of the eddy center between two snapshots divided by the time between the snapshots. As the outer shape of the eddies is defined on a discrete grid, the eddy radius R may fluctuate between two grid cells and therefore may change by the distance between two grid cells between two time steps. In order to avoid these fluctuations that result solely from the discrete grid, the eddy radii R and areas A are filtered with a 7 day moving average ($\pm$3 days) along the respective eddy trajectories. For the two model simulations, a 10 day moving average is used ($\pm$5 days, i.e., $\pm$1 output time step).

2.4. Surface Temperature Anomalies and Temperature Fluxes of Individual Eddies

We seek to combine the results from the eddy detection with sea surface temperature (SST) data in order to investigate the temperature flux associated with the eddies' movements across 47°N. While Argo data and ship-based observations may provide insight into the vertical structure of eddies and add salinity measurements, the available data from the deep ocean is scarce in space and time compared to surface-limited satellite observations. As we presently lack appropriate data to infer the vertical structure of the eddies at a similar temporal and spatial resolution as at the surface, we focus on the two-dimensional analysis of surface anomalies and surface fluxes related to the eddies.

For the observations, we use daily data from the NOAA 1/4° × 1/4° Optimum Interpolation Sea Surface Temperature version 2 (OISST V2) analysis [*Reynolds et al*., 2007] and combine it with the eddy shapes detected in the daily AVISO geostrophic velocity fields. The SST data set is based on satellite observations with the Advanced Very High Resolution Radiometer (AVHRR) and corrected with in situ measurements from ships and buoys. We calculate the two-dimensional temperature flux carried by individual eddies ($\vec{Q}$ [W m^{-1}], with 1 GW m^{-1} = 10^9 W m^{-1}) as follows:

$$\vec{Q}=\vec{u}_E \cdot 2R \cdot \rho_0 \cdot c_{p_0} \cdot \overline{SST'}, \tag{2}$$

where $\vec{u}_E$ is the eddy's translation velocity, R is the radius of the individual eddy, ρ_0=1025 kg m^{-3} an average seawater density, c_{p_0}=4200 J kg^{-1} K^{-1} an average-specific heat capacity for seawater, and $\overline{SST'}$ is the average of all SST anomaly grid points within the area ($A=\pi R^2$) of the eddy. The daily SST anomaly at each

Table 1. List of Cruises Carried Out Between 2003 and 2014 With LADCP Stations Along 47°N

Ship and Cruise	Period of LADCP Sections Along 47°N	No. LADCP Profiles	Longitudinal Range of Section
Meteor M59/2	16–26 Aug 2003	45	44°W–13°W
Thalassa SUBPOLAR	4 Jun to 12 Jul 2005	30	43°W–10°W
Maria S. Merian MSM5/1	28–30 Apr 2007	13	44°W–41°W
Maria S. Merian MSM9/1	4–10 Aug 2008	27	44°W–29°W
Maria S. Merian 12/3	30 Jul to 5 Aug 2009	26	47°W–31°W
Meteor M82/2	6–28 Aug 2010	45	47°W–15°W
Meteor M85/1	25 Jun to 16 Jul 2011	44	47°W–11°W
Maria S. Merian MSM21/2	8–14 Jul 2012	31	47°W–31°W
Maria S. Merian MSM27	20–22 Apr 2013	16	47°W–43°W
Maria S. Merian MSM28	29 May to 14 Jun 2013	39	44°W–11°W
Maria S. Merian MSM38	19 May to 28 May 2014	51	47°W–29°W

grid point is calculated with respect to the mean annual cycle at the respective grid point. This is done to remove the dominant seasonal signal, since we are only interested in the influence of the eddy on the temperature anomaly and not in the mean seasonal cycle of the SST at the respective point. Calculating the anomaly with respect to the surrounding water yields somewhat different numbers for individual eddies but does not change the overall results. Unlike the velocity field, the SST is not interpolated to 1/6° × 1/6° resolution, as this was done for the velocities only to improve the performance of the eddy detection algorithm. The temperature flux calculated here can be seen as a heat flux relative to a varying reference temperature (i.e., the mean seasonal cycle of the temperature).

For the model simulations, we use the SST field from the respective model run instead of the OISST, but the calculation of the surface temperature flux for eddies detected in the model is exactly the same as for the observations. The structures of the mean SST fields of both model simulations are very similar to the mean SST field derived from observations, clearly showing the cold subpolar gyre and the warm subtropical gyre (Figure 1). However, both model simulations show warmer temperatures north-west of the Northwest Corner when compared to the observations, and the SST field in the ANHA4 simulation is smoother than the observations.

2.5. Shipboard Velocity Observations

Top to bottom profiles of current velocity from lowered Acoustic Doppler Current Profilers (LADCP) measurements were obtained on 11 research cruises. These were carried out nominally along the 47°N section between 2003 and 2014. All 11 sections included the western basin and the continental slope, while only 5 of them (2003, 2005, 2010, 2011, and 2013) extended all the way to the eastern basin. In the western basin the cruise tracks typically start at Flemish Pass and nominally follow 47°N. In the eastern part of the section, the tracks deviate from the 47°N section and are inclined northward toward the shelf where they end around Goban Spur (Figure 1a). The shelf regions on either side of the Atlantic are not covered by LADCP data. All cruises and the extent of the respective velocity sections along 47°N are summarized in Table 1. Measurements were taken with two LADCP-devices of the type Teledyne RDI 300 kHz Workhorse Monitor. The instruments were operated in a synchronized mode with a ping rate of 1 Hz and a vertical bin size of 10 m. The processing of the raw data follows *Visbeck* [2002]. All LADCP profiles were detided using the TPXO7.2 tidal model [*Egbert and Erofeeva*, 2002] and then linearly interpolated onto a regular grid with a horizontal resolution varying between 4 km at the continental slope and 40 km in the interior ocean and a vertical resolution of 10 m. Data from the western basin west of 36°W prior to 2012 have already been used by *Mertens et al.* [2014] to calculate the NAC transport, WBC transport, and the strength of the recirculation in the Newfoundland Basin (NBR).

3. Distribution and Characteristics of Eddies

3.1. Spatial Distribution of Eddies Detected in the Altimeter Data

To investigate whether or not EKE in the study region is mainly caused by individual eddies, we relate the spatial distribution of eddies to the spatial distribution of EKE in the area averaged over the period of interest (Figure 3a). The EKE is computed as $\frac{1}{2}(u'2+v'2)$, where primes denote deviations from the mean annual cycle, so that it includes all intraseasonal components of the kinetic energy. The highest levels of EKE in the

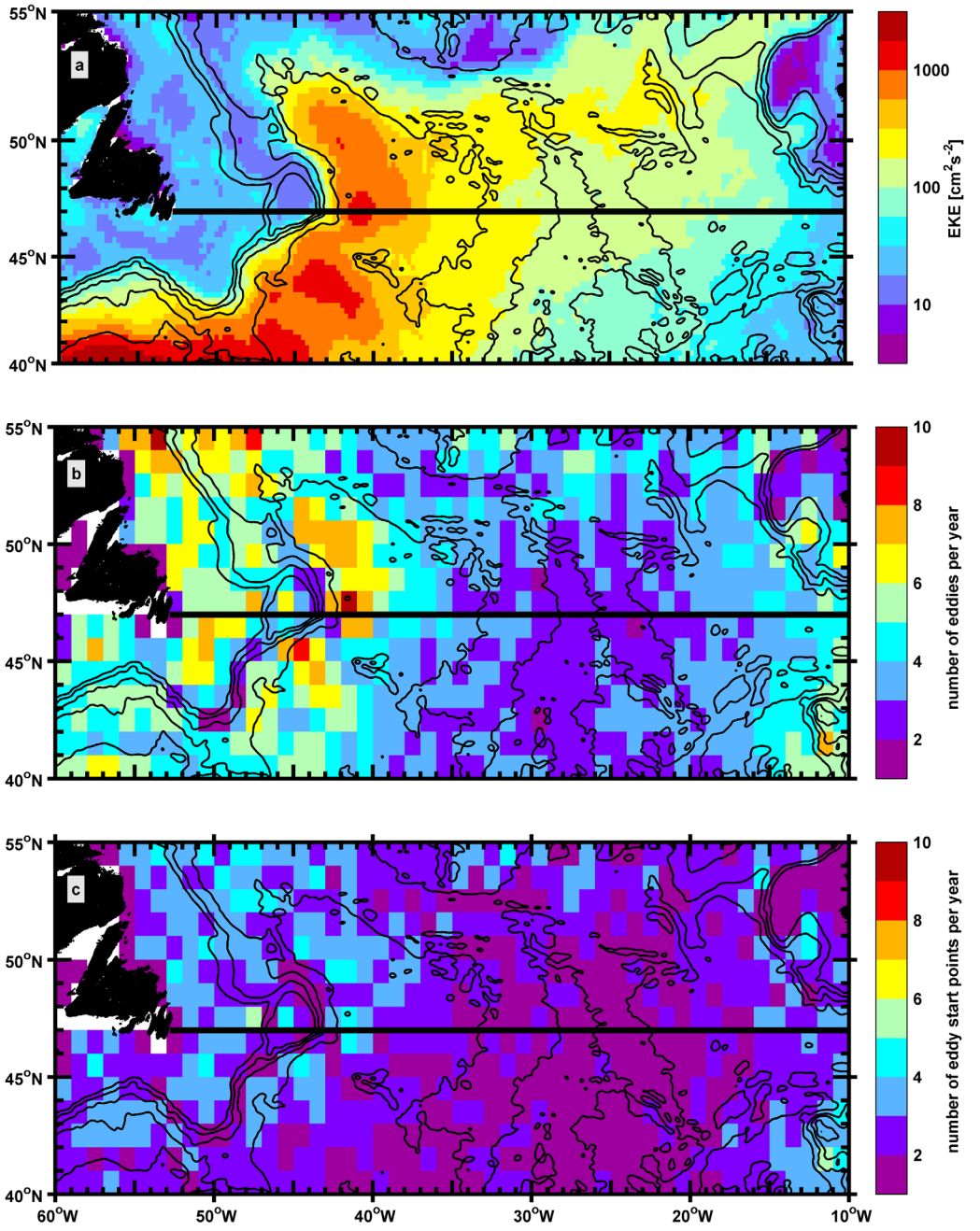

Figure 3. (a) Mean eddy kinetic energy (EKE) derived from geostrophic velocity anomalies compared to a (b) map of the number of detected eddies per year and the (c) number of eddy start points per year from January 1993 to April 2014 binned in 1° × 1° boxes. Note that EKE [cm^2/s^2] is shown with a logarithmic scale. Isobaths are given every 1000 m using low-pass-filtered bathymetry derived from the ETOPO1 data set [*Amante and Eakins*, 2009].

study region are found along the pathway of the NAC all the way up to the Northwest Corner. Local maxima of EKE (>1000 cm^2 s^{-2}) are visible south of the Grand Banks of Newfoundland, around 44°N at the northern side of the Mann-Eddy, and around 47°N east of the Flemish Cap (Figure 3a). The region of elevated EKE then widens and spreads toward the eastern basin following the pathway of the NAC over the fracture zones at the MAR. In contrast, the western side of the region is characterized by a strong EKE gradient following the continental slope of the Grand Banks of Newfoundland and low EKE in the order of 10–100 cm^2 s^{-2} on the shallow shelf.

In the satellite observation period January 1993 to April 2014 we find a total of 36,997 eddies (∼1800/year) with a lifetime of more than 7 days and a radius larger than $R_{min}=20\times cos(\phi)$ km in the region between 60°W–10°W and 40°N–55°N. In order to assess the distribution of the detected eddies in the study region, the number of eddy centers in each 1° × 1° box is counted. An eddy is counted once for a box no matter how long its center remained inside the respective box (Figure 3b). The eddy will be counted again when entering a different box, thus just summing up the numbers of all boxes will not result in the total number of eddies. The highest numbers of eddies are found in the western basin along the NAC pathway and on the Grand Banks of Newfoundland. Along the NAC pathway eddies follow roughly the 4000 m isobath along the Grand Banks with regional maxima of 8–10 eddies per year north of the Mann-Eddy and east of the Flemish Cap. The band of abundant eddies then continues toward the Northwest Corner with around six to eight eddies per year. The shelf break where the bathymetry is steepest shows fewer eddies than the surroundings while the shallow shelf region again shows numbers between five and eight eddies per year. The trace of elevated numbers of eddies then follows the NAC eastward and forms a narrow band around 52°N close to the fracture zones of the Mid-Atlantic Ridge (MAR). The MAR region south of 50°N shows less eddy activity with only one to three eddies per year. Higher numbers (five to eight eddies per year) are also observed along the shelf region in the eastern basin, especially on the shelf of the Iberian Peninsula and the southern Irish shelf. Only counting the boxes where eddies first appear results in a very similar pattern, even though the numbers are self-evidently lower. Most eddies are first detected along the boundary between NAC and WBC, in the region north-west of the Northwest Corner, on the North American shelf and along the eastern boundary of the basin (Figure 3c).

Comparing the distribution of detected eddies with the average EKE in the area, we find that regions of eddy occurrences and regions of the highest EKE do not necessarily coincide. While some local maxima of EKE indeed coincide with local maxima of eddy occurrence, many features in the EKE distribution cannot be explained by eddies. In fact, we can identify only few eddies in the regions where we find the highest EKE, especially south of the Grand Banks of Newfoundland between 40°N and 45°N. This suggests that the high EKE is caused by other processes (e.g., shifting of the mean NAC pathway, and meandering of the NAC) rather than by individual eddies.

Despite similar or even higher spatial resolution in the model simulations, we find fewer eddies (11,397 in ANHA4 (∼950/year) and 14,501 in ANHA4-SPG12, ∼1200/year) for the period January 2002 to December 2013 than in the observations for the same period (20,267, ∼1700/year). The overall distribution is similar though, with the highest number of eddies along the pathway of the NAC. Only the shelf regions of the Grand Banks of Newfoundland show substantial differences where unlike in the observations, we find only very few eddies in both of the model simulations.

3.2. Comparison of Eddy Characteristics Between Observations and Model

We are interested in the typical characteristics of eddies as well as the variability of eddy characteristics within the study region between 60°W–10°W and 40°N–55°N. All numbers displayed here are given as the mean value of all eddies in the study region. The variability is represented by the inner quartile range (i.e., the range of 50% of the values, shown in brackets). The standard errors of the mean values within a 90% confidence interval (SEM) are calculated by bootstrapping the mean value with 1000 iterations. For the comparison of the observations with the two model simulations, we focus only on the model period ranging from January 2002 to December 2013. The mean value and the variability of all characteristics of the eddies from satellite observations remain essentially the same as for the full observation period January 1993 to April 2014. All eddy properties are listed in Table 2, and the respective probability density functions (PDFs) are shown in Figure 4.

The radius and lifetime of eddies in the two model simulations are essentially independent of the respective horizontal resolution of the model and do not differ substantially between the two model setups (Table 2). At around 36 km the average eddy radius in the models is somewhat smaller than in the observations (42 km), and the average eddy lifetime in the models (about 1 month) is 1 week longer than in the observations (23 days, Table 2). These differences are also clearly visible in the PDFs for radii and lifetimes (Figures 4a and 4b). Especially the distinct tail with high probabilities for long eddy lifetimes in the model simulations, compared to the peak of shorter lifetimes in the observations, is clearly recognizable. The observed spatial distribution of eddy radii shows a similar pattern as the spatial variation of the first Rossby radius of

Table 2. Characteristics of Eddies Detected in the Region Between 60°W and 10°W and 40°N and 55°N for Observations and Model Experiments With Different Horizontal Resolutions[a]

	Observations		Model	
			ANHA	ANHA4-SPG
Period	Jan 1993 to Apr 2014	Jan 2002 to Dec 2013	4 Jan 2002 to Dec 2013	12 Jan 2002 to Dec 2013
Total number of detected eddies	36,997	20,267	11,397	14,501
Radius [km]	41.3 [32.3, 47.5] (0.02)	41.7 [32.6, 47.9] (0.03)	36.2 [27.0, 43.0] (0.06)	36.2 [28.4, 42.2] (0.05)
Lifetime [days]	22.5 [10, 26] (0.2)	23.0 [10, 26] (0.2)	31.4 [20, 35] (0.3)	33.4 [20, 40] (0.3)
Translation speed [cm s^{-1}]	4.1 [1.9, 5.7] (0.02)	4.1 [1.9, 5.7] (0.03)	2.0 [1.1, 2.8] (0.02)	2.6 [1.5, 3.6] (0.02)
Travel distance [km]	73 [23, 95] (0.5)	74 [23, 95] (0.7)	58 [19, 80] (0.7)	80 [27, 108] (0.8)

[a]Only eddies with a lifetime of more than 7 days and a radius >20 km $\times\cos(\phi)$ (where ϕ is the latitude) are taken into account. The variance of the values is represented by the inner quartile range (i.e., 50% of the values, shown in brackets). The standard error of the mean value within a 90% confidence interval (given in parentheses) was calculated from bootstrapping the mean value with 1000 iterations.

deformation derived by *Chelton et al*. [1998]. Both eddy and Rossby radius vary with latitude and water depth and the eddy radius is about 1.5–2 times the Rossby radius. We find a correlation of 0.8 when comparing the local eddy radius with the local Rossby radius of deformation (both binned in $1^\circ \times 1^\circ$ boxes).

Contrary to eddy radii and lifetimes, estimates regarding the number of eddies detected in the region, the average translation speed, and the average travel distance do depend on the respective horizontal resolution of the model grid. The respective PDFs differ substantially between the two simulations (Figures 4c and 4d). There are more eddies in ANHA4-SPG12 than in ANHA4, they move faster (2.0 [1.1, 2.8] cm s^{-1} in ANHA4, and 2.6 [1.5, 3.6] cm s^{-1} in ANHA4-SPG12) and travel longer distances (58 [19, 80] km in ANHA4 and 80 [27, 108] km in ANHA4-SPG12). While the average travel distance of eddies in the models is in a similar range as that of the altimeter-derived eddies (72 [23, 95] km), the eddy translation speed in the models is only around 50–60% of the observed speed. The PDF for the translation speeds shows long tails for the observations compared to a rather sharp drop for the two model simulations (Figure 4c), likely caused by the different temporal resolutions (5 days in the model versus daily for the observations).

The variability of the above mentioned properties (except the eddy radius) is always higher in the ANHA4-SPG12 simulation and decreases when the horizontal resolution of the model grid is coarser. Overall, the eddy characteristics in the higher-resolution 1/12° ANHA4-SPG12 simulation are closer to those of the altimeter-derived eddies than the 1/4° ANHA4 simulation, even though the latter has the same resolution as the observations.

4. Temperature Fluxes of Individual Eddies Crossing 47°N

We focus now on the temperature flux ($\vec{Q}$ as defined in equation (2)) across the zonal section at 47°N. We identify all eddies crossing the section between 53°W (Newfoundland) and 10°W and merge the surface temperature fluxes of the eddies at the time of the crossing into a time series of temperature fluxes covering the period January 1993 to April 2014 for the observations and January 2002 to December 2013 for the two model simulations, respectively (Figure 5). Four different cases will be considered separately: (i) warm eddies moving northward, (ii) cold eddies moving southward, (iii) cold eddies moving northward, and (iv) warm eddies moving southward. Cases (i) and (ii) result in a positive (northward, Q_N) temperature flux, while cases (iii) and (iv) lead to a negative (southward, Q_S) temperature flux. As for the previous analysis, all numbers displayed here are given as a mean value, and the variability is represented by the inner quartile range. All numbers together with the SEM within a 90% confidence interval are listed in Table 3. The SEM was calculated by bootstrapping the mean value with 1000 iterations.

In the observations between January 1993 and April 2014, we detect a total of 823 eddies with a lifetime of more than 7 days and radius larger than $R_{\min}=20\times cos(\phi)$ that cross 47°N (Figure 5a). The average travel distance of eddies after crossing 47°N is around 80 km, with about 1/3 of all eddies traveling further than 100 km. Of the detected eddies, 51% moved northward, and 49% moved southward. Similarly, 52% (48%) have a positive (negative) temperature flux. Also the sense of rotation (52% anticyclones, 48% cyclones) and the type of SST anomaly (48% warm, 52% cold) were evenly distributed. While there is no dominance

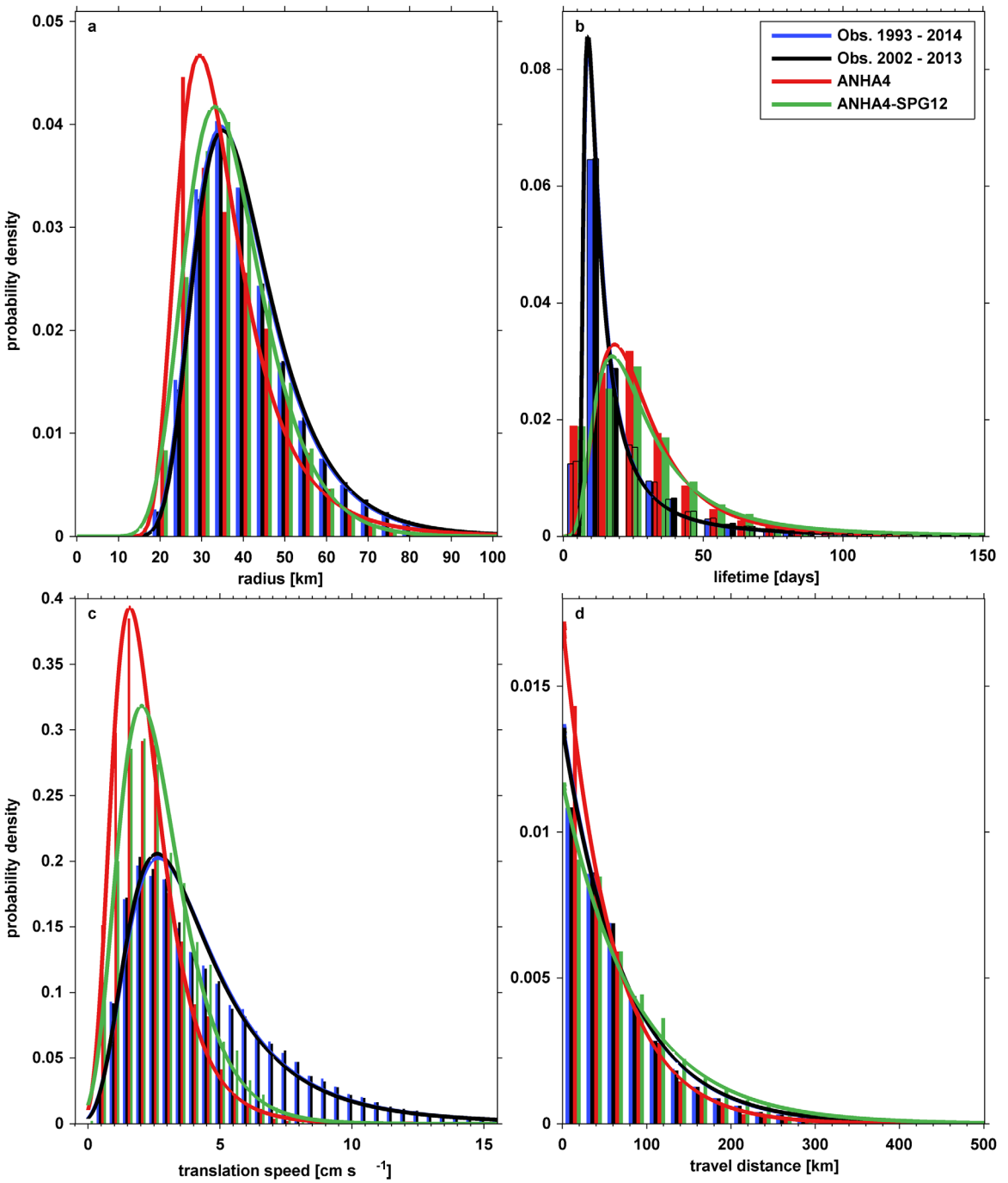

Figure 4. Probability density of characteristics associated with eddies detected between 60°W and 10°W and 40°N and 55°N in observations and two model simulations; (a) radius, (b) lifetime, (c) translation speed, and (d) travel distance. Only eddies with a lifetime of more than 7 days and a radius >20km $\times\cos(\phi)$ (where ϕ is the latitude) are taken into account. Due to the different temporal resolution of the observations (daily) and the model runs (5 days), the bar plots of the lifetimes in Figure 4b have different bins that overlap sometimes. For Figures 4a–4c the probability distributions fitted to the histograms is a generalized extreme value distribution. The fit for the distribution of the travel distance in Figure 4d is exponential.

of any type of eddy, there is a clear connection between the sense of rotation and the temperature anomaly carried by the eddy. The majority (58%) of anticyclones crossing 47°N are related to a warm SST anomaly, while the majority of cyclones (63%) have a cold SST anomaly.

The temperature flux across 47°N varies substantially between different eddies (Figure 5a and Table 3). Since northward and southward fluxes often cancel out each other, the net flux is small even though there

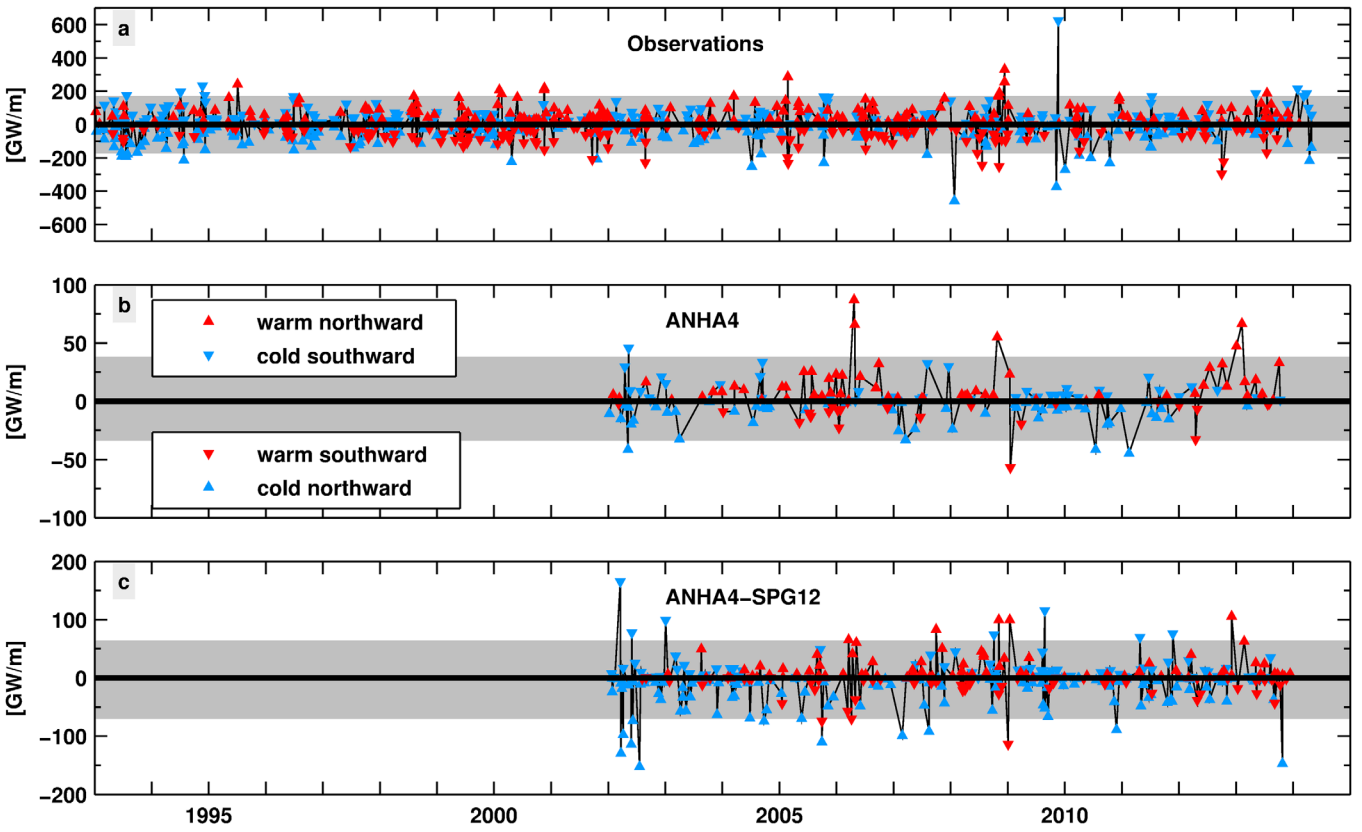

Figure 5. (a) Time series of the meridional temperature flux by eddies across the zonal section at 47°N in the observations, (b) 1/4° ANHA4 simulation, and (c) 1/12° ANHA4-SPG12 simulation, 1 GW $m^{-1} = 10^9$ W m^{-1}. Red (blue) triangles indicate eddies with a warm (cold) SST anomaly. The direction of the triangle indicates the direction of meridional eddy movement across 47°N (northward/southward). A positive (northward) temperature flux can be achieved by northward moving warm eddies as well as southward moving cold eddies (and vice versa for a negative temperature flux, see text for details). The gray areas indicate 2 times the standard deviation of each time series. Note that the figures have different vertical scales.

Table 3. Number of Eddies Crossing 47°N and the Respective Temperature Fluxes[a]

	Observations		Model	
			ANHA4	ANHA4-SPG12
Period	Jan 1993 to Apr 2014	Jan 2002 to Dec 2013	Jan 2002 to Dec 2013	Jan 2002 to Dec 2013
Total number of eddies	823	437	182	360
Number of strong eddies	46 (5.6%)	26 (5.9%)	10 (5.5%)	26 (7.2%)
Number of regular eddies	777	411	172	334
Eddy radius [km]				
Regular eddies	42.1 ± 11.0	42.6 ± 11.9	37.5 ± 11.0	36.1 ± 9.2
Strong eddies	50.6 ± 12.7	52.4 ± 13.0	45.6 ± 15.4	42.4 ± 8.7
Transl. speed [cm s^{-1}]				
Regular eddies	20.4 ± 3.9	20.0 ± 4.2	5.2 ± 2.3	4.9 ± 2.8
Strong eddies	21.4 ± 1.5	21.4 ± 2.0	8.6 ± 2.9	9.6 ± 2.3
$\lvert SST' \rvert$ [°C]				
Regular eddies $\lvert SST'_r \rvert$	0.7 ± 0.5	0.7 ± 0.5	0.6 ± 0.5	0.8 ± 0.8
Strong eddies $\lvert SST'_s \rvert$	2.6 ± 0.9	2.8 ± 1.0	1.9 ± 0.6	3.0 ± 1.0
Q_N [GW m^{-1}]	60.1 [21.0, 82.7] (3.7)	59.4 [19.3, 82.7] (5.4)	12.8 [3.2, 17.1] (2.0)	17.7 [2.1, 21.3] (2.5)
% by strong eddies	18%	16%	29%	37%
Q_S [GW m^{-1}]	−64.0 [−86.7, −19.7] (3.9)	−63.3 [−77.5, −16.6] (6.2)	−11.0 [−14.6, −3.9] (1.6)	−21.4 [−31.4, −2.3] (2.7)
% by strong eddies	24%	34%	21%	35%
$\bar{Q}$ [GW m^{-1}]	0.5 [−46.8, 44.6] (3.9)	1.5 [−39.0, 45.1] (5.5)	2.2 [−6.2, 8.2] (1.7)	−2.8 [−9.2, 6.7] (2.3)
% by strong eddies $(\sum \lvert Q_{strong} \rvert / \sum \lvert Q_{all} \rvert)$	21%	25%	25%	36%

[a]The variance shown in brackets represents the inner quartile range (i.e., the range of 50% of the values). The uncertainty of radius, translation speed, and SST anomaly are given as one standard deviation. The standard error of the mean value within a 90% confidence interval (given in parentheses) was calculated from bootstrapping the mean value with 1000 iterations. See text for the definition of strong eddies.

are large fluxes in both direction. Here the mean flux in either direction is around ± 60 GW m^{-1}, while averaging over all eddies results in a mean net flux $\bar{Q}$ that is effectively zero (0.5 [–46.8, 44.6] GW m^{-1}).

A substantial fraction of the temperature flux in either direction is achieved by eddies with an anomalously high-temperature flux. We define these so-called "strong eddies" as all those eddies with a temperature flux that exceeds the mean flux plus two times the standard deviation in either direction ($\bar{Q} \pm 2 \times \sigma(Q)$, where the overbar denotes the mean, and σ is the standard deviation, Figure 5). All other eddies are defined as "regular eddies."

Since the mean net flux is so small, it can be more practical to look at the absolute values of flux (i.e., without regard of the direction). The absolute temperature flux by eddies is calculated as the sum of the fluxes of all eddies without regard for the direction of the flux, i.e., $\sum_i |Q_i|$. While this does not tell anything about the net effect of eddies, it gives us an idea about the overall strength of fluxes, their contribution to the variability, and the contribution of strong eddies to the total flux by eddies (i.e., $\sum |Q_{strong}| / \sum |Q_{all}|$).

While only 46 out of 823 eddies are strong eddies (5.6% of all eddies), these strong eddies make up for 21% of the absolute temperature flux across 47°N (18% of the northward and 24% of the southward flux). This means that an average strong eddy ($\overline{|Q_{strong}|}$) accounts for 4–5 times of the temperature flux of regular eddies ($\overline{|Q_{regular}|}$).

As for the whole domain, we find fewer eddies crossing 47°N in the model simulations from January 2002 to December 2013 than in the observations for the same period (Figures 5b and 5c and Table 3). The mean temperature fluxes in either direction are substantially lower in both model simulations than in the observations (~20% in ANHA4, e.g., 12.8 versus 59.4 GW m^{-1} for mean northward flux, Table 3; ~30% in ANHA4-SPG12). We therefore focus on the relative contribution of strong and regular eddies to the temperature flux since it is well represented in both model configurations.

Also, the variability of the temperature fluxes relative to the respective mean is comparable between observations and models (Table 3). Considering only the model period from January 2002 to December 2013 for the satellite observations, 5.9% (26 out of 437) of the altimeter-derived eddies are strong eddies, and they account for 25% of the observed absolute temperature flux by eddies.

In the ANHA4 simulation we detect 182 eddies of which 10 (5.5%) are strong eddies. The mean flux in either direction is around 11–12 GW m^{-1} and the mean net flux across 47°N is 2.2 [–6.2, 8.2] GW m^{-1}. Strong eddies account for 25% of the absolute temperature flux by eddies, supporting the findings in the satellite observations.

In the ANHA4-SPG12 simulation, we detect 360 eddies of which 26 (7.2%) are strong eddies. Here the contribution of strong eddies is higher than in the observations, accounting for 36% of the absolute temperature flux by eddies. The temperature flux by eddies in both directions is larger than in the ANHA4 simulation (around 18–21 GW m^{-1}, Table 3), and the mean net flux is directed southward (-2.8 [–9.2, 6.7] GW m^{-1}).

Following equation (2), three parameters (translation speed $\vec{u}_E$, radius R, and SST anomaly $\overline{SST'}$) have to be taken into account as possible causes for the anomalously high-temperature flux of strong eddies. The values for $\vec{u}_E$, R, and $\overline{SST'}$ (mean $\pm$ one standard deviation) are listed in Table 3.

Translation speed ($\vec{u}_E$). The average meridional translation speed of strong eddies crossing 47°N is larger than that of regular eddies. This difference is negligible small in the observations. In the model simulations the difference is more pronounced with regular eddies moving substantially slower (almost by a factor of two) than strong eddies (Table 3). Nevertheless, these differences are not large enough to explain the notable difference in temperature flux between regular and strong eddies.

Eddy radius (R). For the observations and both model simulations, strong eddies crossing 47°N are 1.2 times larger than regular eddies (Table 3). While this can explain a small fraction of the difference in temperature flux between regular and strong eddies, the difference in radii are not large enough to explain the anomalously high-temperature flux of strong eddies.

SST anomaly ($\overline{SST'}$). Most importantly, strong eddies show a substantially higher-temperature anomaly than regular eddies. The composite fields of the SST anomalies surrounding strong and regular eddies are shown in Figure 6. The average SST anomaly (not regarding the sign of the anomaly) of altimeter-derived strong eddies crossing 47°N ($|T_s| = 2.6 \pm 0.9^{\circ}$C) is almost 4 times colder/warmer than that of regular eddies

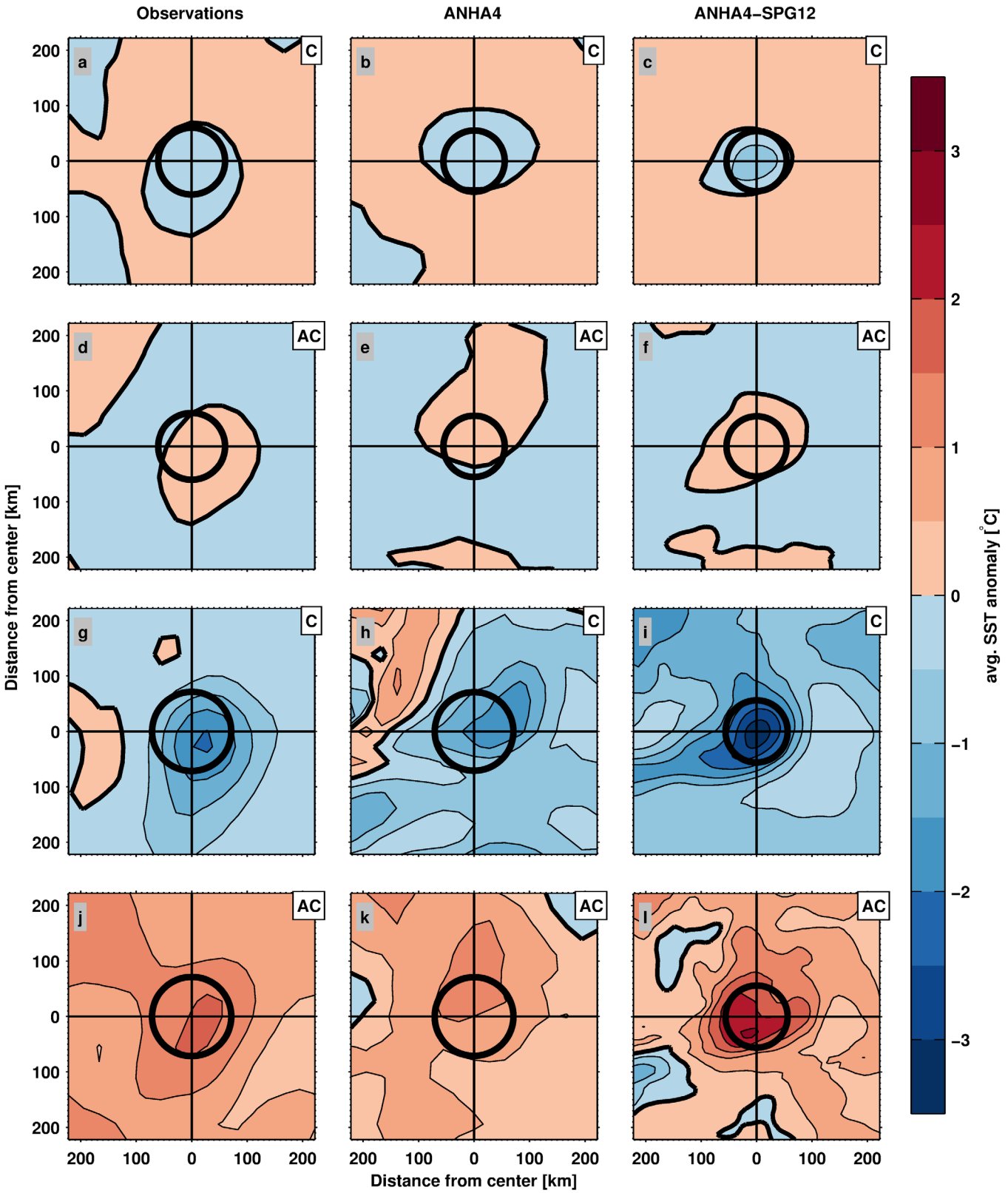

Figure 6. Composite of the average SST anomaly associated with eddies crossing 47°N in the observations (left column), 1/4° ANHA4 simulation (center column) and 1/12° ANHA4-SPG12 simulation (right column) for (a–c) regular cyclonic, (d–f) regular anticyclonic, (g–i) strong cyclonic, and (j–l) strong anticyclonic eddies. The number of eddies used to calculate the respective composites differs for each case. The black circle indicates the average eddy radius with a 95% confidence interval.

($|T_r|$=0.7±0.5°C, Figure 6). The SST anomaly of strong eddies is even stronger related to the sense of rotation of the eddy than it is for regular eddies. For strong altimeter-derived eddies, 80% of the anticyclones are related to a warm SST anomaly, and 80% of cyclones are related to a cold SST anomaly. This behavior is again supported by the model simulations. The average SST anomaly of strong eddies in the ANHA4 simulation is $|T_s|$=1.9±0.6°C, compared to $|T_r|$=0.6±0.5°C for regular eddies. For the strong eddies in the ANHA4 simulation, six of the eight anticyclones are related to a warm SST anomaly, and two out of two cyclones are related to a cold SST anomaly. In the ANHA4-SPG12 simulation strong eddies have an average SST anomaly of $|T_s|$=3.0±1.0°C, compared to $|T_r|$=0.8±0.8°C for regular eddies. Similar to the observations and the ANHA4 simulation, 6 out of 7 strong anticyclones are related to a warm SST anomaly, and 13 out of 13 strong cyclones are related to a cold SST anomaly.

All in all, we find that a small number of strong eddies, which are associated with a larger SST anomaly than regular eddies, are responsible for about 25% of the absolute temperature flux by eddies across 47°N and therefore greatly contribute to the exchange of cold/warm water masses across 47°N. This result is consistent between the observations and the two model simulations with different horizontal resolutions.

5. Pathways of Eddies Across 47°N in Relation to the Top-To-Bottom Velocity Field

So far we have addressed the temporal variability of the temperature flux by eddies across 47°N. The flux varies not only in time, it also shows considerable regional differences. We therefore analyze the spatial distribution of eddies crossing 47°N to look at main pathways of eddies and areas of strong eddy activity. To relate the identified eddy activity to major branches of the oceanic circulation in the region, we compare the spatial distribution of eddies to vertical sections of the meridional velocities derived from ship surveys and model simulations.

Averaging the direct LADCP measurements obtained on 11 research cruises between 2003 and 2014 yields a composite meridional velocity section along nominally 47°N (Figure 7a). The 12 year means of the meridional velocities from the model simulations are smoother than the composite field in the observations (Figures 7b and 7c). The differences can be explained by the different temporal (12 year mean of 5 daily model data versus average of 11 snapshots) and vertical resolution (between 1 m at the surface and hundreds of meters in the deep ocean in the model versus 10 m in the observations). Nevertheless, the main structures of the meridional velocity are well reproduced in both model simulations and consistent with the observations (Figure 7). The eastern shelf region is visible in the observations (Figure 7a) but not in the model simulations (Figures 7b and 7c), because the ship tracks deviate from the 47°N latitude and are inclined northward toward the shelf (Figure 1a).

The western boundary region with the WBC, the NAC and the NBR, is characterized by the highest meridional velocities and strong horizontal shear in the observation and both model simulations (Figure 7). The structures in the velocity field in this region are surface intensified but extend down through the whole water column. This behavior and the average position of the three features are consistent between observations and both model simulations. The structure of the WBC is well reproduced in the ANHA4-SPG12 simulation, showing two distinct velocity cores at the continental slope and rise as in the observations [*Mertens et al.*, 2014]. In contrast, the WBC in the ANHA4 simulation consists of only one core and is generally weaker with lower velocities and smaller spatial extent. The flow reversal in the Flemish Pass at 47°N, with a strong southward core in the west and a weaker northward flow at the western flank of the Flemish Cap is well reproduced in both model simulations. The regions over the MAR and the eastern basin show less spatial variability in the model simulations than in the observations. Note that the eastern part of the section was only covered by 5 of the 11 cruises (Figure 1a and Table 1). The average of the LADCP measurements is thus less robust than in the western part of the section.

For the analysis of the main eddy pathways the number of eddies crossing 47°N are binned into 1° intervals, each centered around one longitude (Figure 8). The respective temperature fluxes within each bin are summed up to a net (sum of all eddies), a net regular (sum of only regular eddies) and a net strong flux (sum of only strong eddies). In many cases the net regular flux is small, because the northward and southward flux of regular eddies within one bin cancel out each other (Figure 9). The direction of the net flux is therefore in most cases dominated by the net strong flux within the respective bin. Because of the different length of data periods in observations and model, our focus lies on the relative contribution of strong

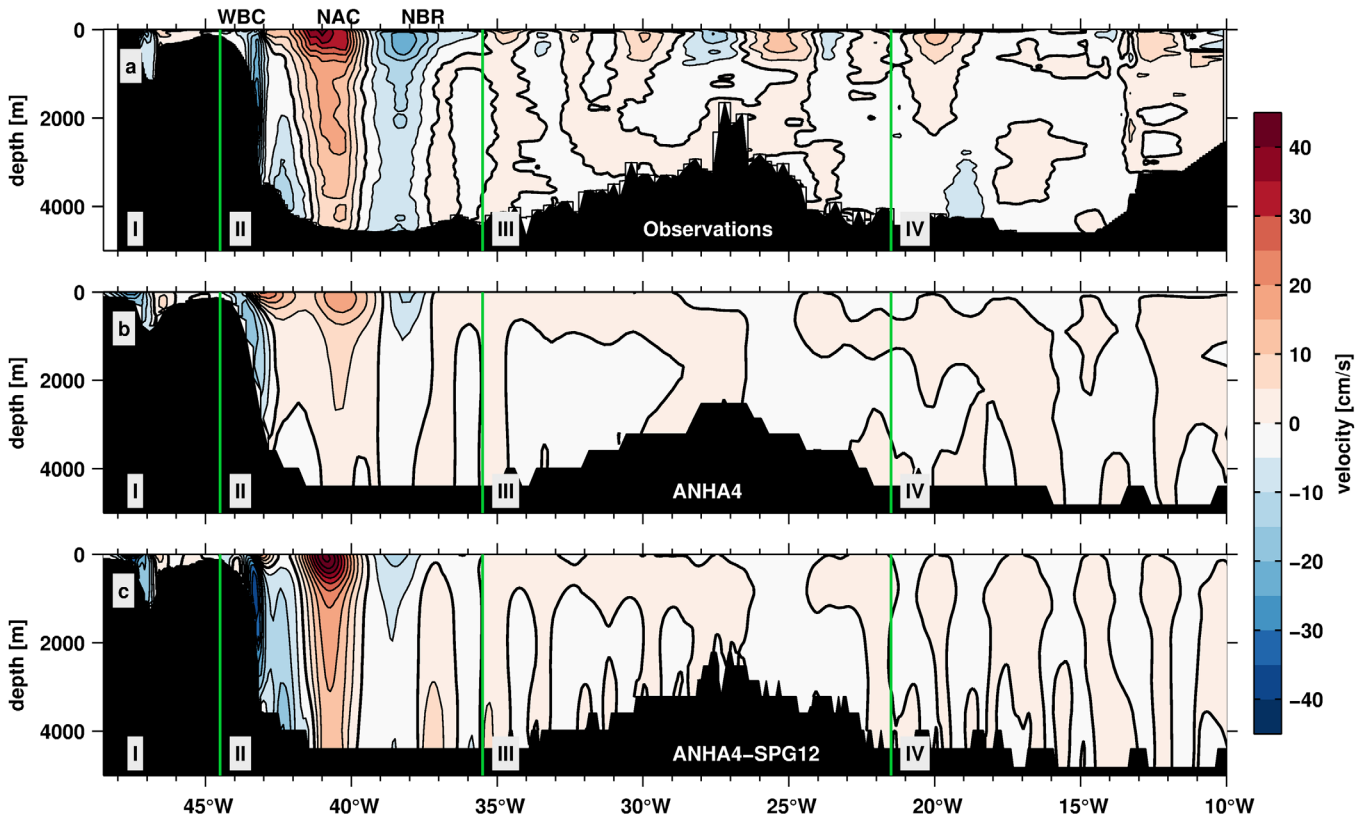

Figure 7. (a) Meridional velocity field along 47°N in the observations, (b) 1/4° ANHA4 simulation and (c) 1/12° ANHA4-SPG12 simulation. For the observations, snapshots from LADCP measurements obtained on 11 research cruises between 2003 and 2014 are averaged. For the model simulations, the mean velocity for the period January 2002 to December 2013 is shown. The position of the Western Boundary Current (WBC), the North Atlantic Current (NAC), and the Newfoundland Basin Recirculation (NBR) is indicated on top. The four subsections along 47°N (I, II, III, and IV) separated by green lines are also indicated in each figure.

eddies to the temperature flux of all eddies within each bin and not on the absolute numbers. For a direct comparison, the numbers of each bin are normalized with the length of the time series.

The main eddy pathways are related to the mean background velocity. We therefore separate the section along 47°N into four subsections characterized by different current regimes and different bathymetry (Figure 7) and quantify the fluxes in these subsections. The westernmost subsection I comprises the Grand Banks of Newfoundland, the Flemish Pass and the Flemish Cap and stretches until 44.5°W. Subsection II starts from the eastern slope of the Flemish Cap (44.5°W), includes the WBC, the NAC, and the NBR, and ends at the eastern end of the NBR (35.5°W). The midsection III spans from 35.5°W to 21.5°W comprising the MAR and its flanks with rough topography, while the eastern most subsection IV stretches from 21.5°W to the eastern end of the study region (10°W).

In the observations and both model simulations, the elevated number of eddies and their direction coincides with regions of high average flow velocity (Figure 8). The flow regimes and temperature fluxes by eddies in the different subsections are now discussed in more detail.

5.1. Major Eddy Pathways and Associated Temperature Fluxes

Most eddies, most strong eddies, and the highest variability of temperature flux by eddies across 47°N are found in subsection II between 44.5°W and 35.5°W. A total of 261 eddies cross this subsection between January 1993 to April 2014 (Figure 8b). There is a narrow band with a large number of eddies moving northward with the NAC in this subsection, while the WBC region is dominated by southward moving eddies. The highest number of eddies (74, i.e., 9% of all eddies) is detected in the 1° bin centered at 41°W (Figure 8b).

The spatial pattern of eddy pathways is supported by the ANHA4-SPG12 simulation. Even though the narrow band of northward moving eddies seems slightly shifted westward, the overall pattern of pathways is

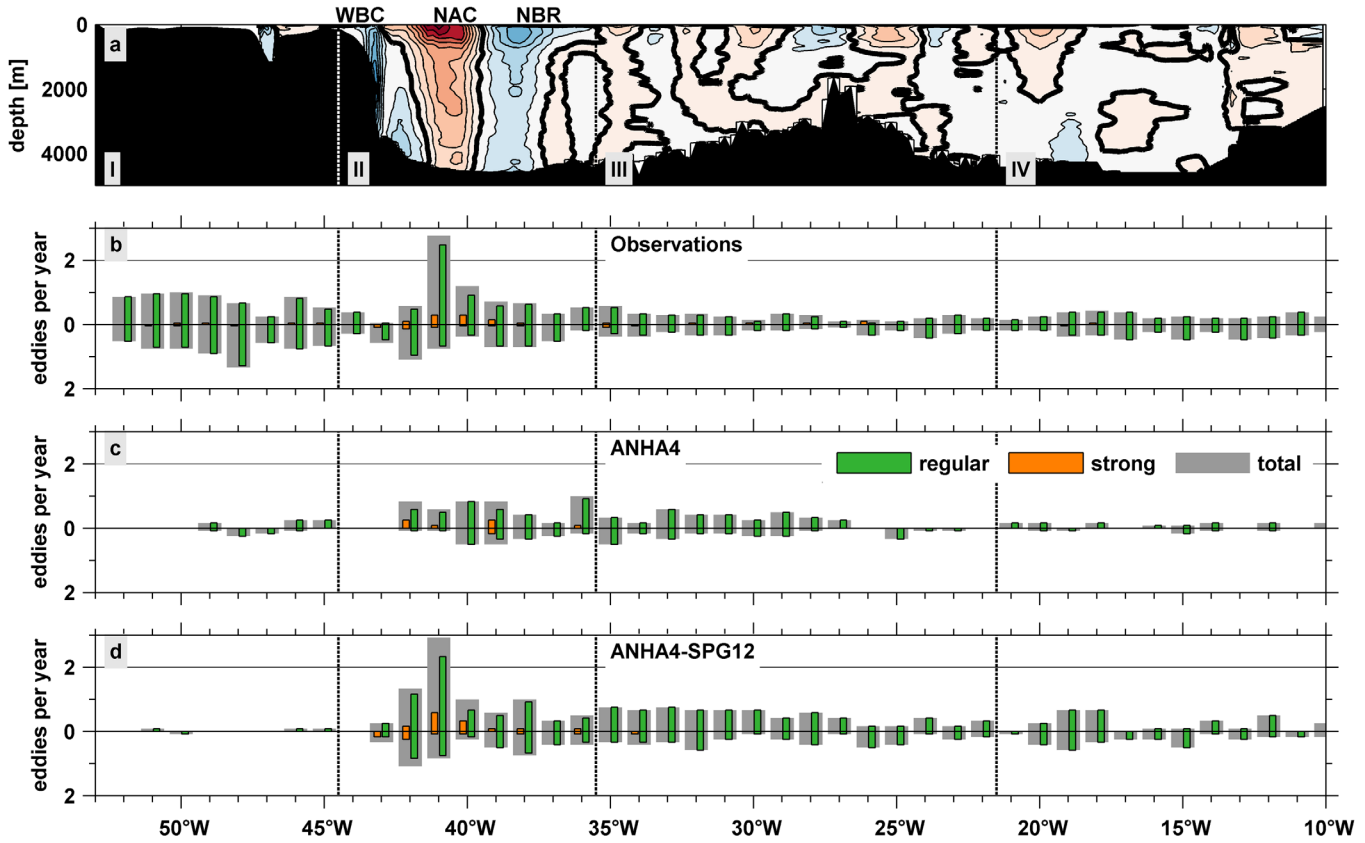

Figure 8. (a) Meridional background velocity from the observations and (b) the number of northward and southward moving eddies per 1° bin crossing 47°N per year in the observations (January 1993 to April 2014), (c) 1/4° ANHA4 simulation (January 2002 to December 2013) and (d) 1/12° ANHA4-SPG12 simulation (January 2002 to December 2013). The total number of eddies in each direction (gray) is separated into regular (green) and strong (orange) eddies.

remarkably similar to that deduced from the from satellite observations (Figure 8c). In ANHA4 there are overall fewer eddies, and the high number of eddies moving northward with the NAC is not reproduced (Figure 8d).

The temperature flux by eddies in either direction is large (>75 GW m^{-1}), leading to a strong variability, while the mean net flux is practically zero (−2.5 [–60.7, 52.0] GW m^{-1}). 28 out of the 261 eddies crossing this subsection are strong eddies. More than 60% (28/46, Table 3) of all strong altimetry-derived eddies are detected in the Newfoundland Basin. These strong eddies in turn account for 34% of the absolute temperature flux of all 261 eddies crossing the subsection (31% of the northward, and 37% of the southward temperature flux, Figure 9b). The importance of strong eddies in the western boundary region is supported by both model simulations. With only one exception at 34°W in the ANHA4-SPG12 simulation, strong eddies in the model simulations occur only in the Newfoundland Basin (Figures 8c and 8d).

In the satellite observations the two bins centered around 40°W and 43°W, respectively, show the two largest southward net temperature fluxes (Figure 9b). These are in turn dominated by the net flux of strong eddies, determining not only the direction but also the magnitude of the net flux. For the bin centered around 43°W, the net flux of strong eddies accounts for 73% of the net flux. In the bin centered around 40°W the southward flux of strong eddies is partially compensated by a northward net flux of regular eddies, and the net flux of strong eddies accounts for 117% of the net flux. This stresses again how important the few strong eddies are for the temperature flux carried across 47°N by individual eddies.

But even though these two intervals both show a southward temperature flux by eddies, the dynamics behind this transport are fundamentally different. The bin centered around 43°W lies within the WBC, and the southward flux is a result of strong warm eddies moving southward (Figure 8b). In the 1° bin centered around 40°W, the majority of eddies move northward with the NAC, but here we still find one of the

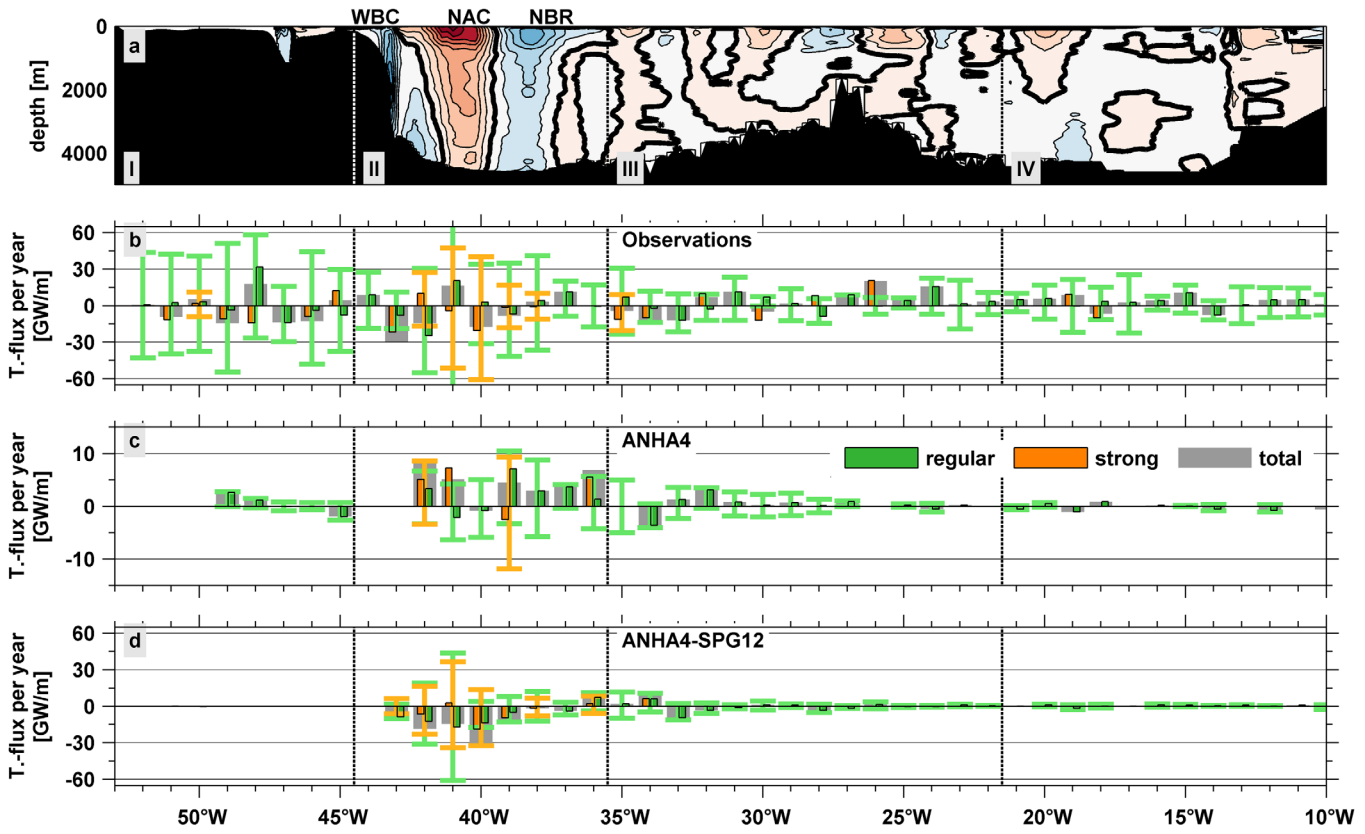

Figure 9. (a) Meridional background velocity from the observations and the (b) sum of the temperature flux by eddies per 1° bin along 47°N (normalized by the number of years) in the observations (January 1993 to April 2014), (c) 1/4° ANHA4 simulation (January 2002 to December 2013), and (d) 1/12° ANHA4-SPG12 simulation (January 2002 to December 2013). The net flux (gray) is separated into fluxes carried by regular (green) and by strong (orange) eddies. Vertical bars show the sum of the temperature flux by eddies of regular (green) and strong (orange) eddies in either direction. The vertical whiskers represent the standard deviation of the respective flux in either direction.

strongest southward temperature flux signals of the whole section (Figure 9b). Responsible for this are strong cyclonic eddies carrying a cold SST anomaly from the WBC northward across the section. The WBC is the only source of subpolar water in the region and one of the main regions where eddies are first detected (Figure 3c). This process is also found in the ANHA4-SPG12 simulation, where strong northward moving cold-core eddies lead to a southward flux between 39°W and 42°W (Figures 8 and 9d).

In the ANHA4 simulation 78 eddies cross the subsection between January 2002 and December 2013, 10 of which are strong eddies. These strong eddies account for 38% of the absolute temperature flux of all identified eddies crossing the subsection (41% of the northward, and 34% of the southward temperature flux by eddies, Figure 9c). In the ANHA4 simulation there are no eddies in the WBC region around 43°W–44°W. This lack of eddies coincides with the weak WBC in the ANHA4 simulation (weaker than in the observations and the ANHA4-SPG12 simulation) and stresses that the eddy pathways coincide with the most pronounced current branches.

In the ANHA4-SPG12 simulation 150 eddies cross the subsection. As for the observations, the highest number of eddies is detected in the 1° bin centered at 41°W. Of the 150 eddies, 15 are strong eddies. These in turn account for 44% of the absolute temperature flux of all identified eddies crossing the subsection (46% of the northward, and 43% of the southward temperature flux). As in the observations, the WBC region shows a southward flux caused mainly by strong southward moving eddies with a warm temperature anomaly. The effect of cold-core eddies moving northward with the NAC and causing a negative temperature flux is even stronger in ANHA4-SPG12 than in the observations, because also the net temperature flux of regular eddies is almost exclusively southward. This confirms the large contribution of cold-core eddies for the overall temperature flux by eddies across 47°N. Both model simulations support the observed large variability in the western basin, with strong fluxes in both directions resulting in a small mean net flux close to zero (4.7 [–7.6, 19.6] GW m^{-1} in ANHA4 and −6.9 [–37.1, 19.1] GW m^{-1} in ANHA4-SPG12).

5.2. Minor Eddy Pathways and Associated Temperature Fluxes

The other three subsections play a minor role for the temperature flux by eddies across 47°N. We find 258, 152, and 132 eddies crossing subsections I, III, and IV, respectively (Figure 8b). The temperature fluxes in either direction in all three regions are lower than in subsection II. They range from 45 to 65 GW m^{-1}, but the resulting mean net temperature fluxes in each subsection are practically zero (Figure 9b). In the model simulations, the respective temperature fluxes in either direction are lower than the observed ones, but the mean net fluxes are also practically zero (Figures 9c and 9d).

One striking difference between observations and the model simulations is the shelf region of the Grand Banks. Unlike in the observations where we detect 132 eddies, there are only 15 eddies detected crossing subsection I in ANHA4 and only 4 eddies at isolated locations in the ANHA4-SPG12 simulation. The other regions are better reproduced by the two model simulations. In the observations we find 68% of all eddies in the MAR subsection crossing 47°N over the western flank of the MAR. This is backed up by the model simulations with even more eddies crossing the subsection over the western flank (91% in ANHA4 and 76% in ANHA4-SPG12). In all cases, more than half of the eddies move northward and these pathways coincide with surface intensified northward background velocities (Figure 7). In the easternmost subsection there are no clearly defined pathways.

Overall, we find that the temperature flux of eddies crossing 47°N shows high spatial as well as temporal variability (denoted by the whiskers in Figures 9b–9d). The largest fluxes as well as the highest variability are observed in the western basin. These findings are coherent in observations and the two model simulations.

6. Discussion and Conclusion

Previous studies have focused on the strength and position of the WBC and NAC and their interaction using results from drifters and floats [e.g., *Rossby*, 1996; *Kearns and Rossby*, 1998; *Carr and Rossby*, 2001; *Dutkiewicz et al.*, 2001; *Bower et al.*, 2009] as well as direct current measurements and hydrographic observations [e.g., *Pérez-Brunius et al.*, 2004; *Kieke et al.*, 2009; *Rhein et al.*, 2011; *Mertens et al.*, 2014]. The southward flow of the WBC, the northward flow of the NAC, and the strength of the anticyclonic recirculation cell east of the Grand Banks have been quantified by *Mertens et al.* [2014] using shipboard and moored current meters along 47°N and the high-resolution (1/20°) VIKING20 ocean model. They have shown that about 2/3 (80 Sv) of the total NAC transport crossing 47°N (110 Sv) are recirculated locally in the Newfoundland Basin, while only about 1/3 (30 Sv) of the northward flow makes it east to cross the MAR [*Mertens et al.*, 2014; *Roessler et al.*, 2015].

While major parts of the large-scale circulation in the interior North Atlantic can now increasingly be quantified, fluxes associated with small-scale features like eddies still need to be addressed. The present study illustrates the importance of individual strong eddies that are linked to a notably large temperature anomaly for the temperature flux by eddies across 47°N. For the eddy detection and the calculation of the respective temperature fluxes, we use data from two completely independent observational data sets (gridded geostrophic velocities provided by AVISO and sea surface temperatures from satellite radiometry), and two model simulations with different resolution, which all show coherent patterns.

The eddy detection algorithm used in this study was designed to be a reliable tool for distinguishing between meanders and eddies [*Nencioli et al.*, 2010]. We are therefore confident that it is a particularly well suited method to detect actual eddies in the study region, where meandering of the NAC plays an important role for the dynamics in the region.

Using a combination of 21 years of geostrophic velocities from satellite altimetry, sea surface temperature data and ship-based velocity measurements, as well as two simulations with the NEMO ocean model with different resolutions spanning a period of 12 years we have found:

1. The highest numbers of eddies in the subpolar North Atlantic are detected along the pathway of the NAC and in the observations also on the shelf of the Grand Banks of Newfoundland (Figure 3).
2. About 25% of the absolute temperature flux by eddies across 47°N stems from eddies with a notably large SST anomaly, so-called strong eddies (Figures 6 and 9).
3. The western part of the Newfoundland Basin with the fastest and most pronounced current branches is the major pathway for eddies and their associated temperature flux across 47°N (Figures 8 and 9).

4. Northward moving cold-core cyclones carrying subpolar water from the WBC make a considerable contribution to the overall temperature flux by eddies in the Newfoundland Basin (Figures 3c and 9).
5. The eastern basin of the North Atlantic at 47°N shows a low temperature flux carried by eddies (Figure 9).
6. While the number of detected eddies is lower in both model simulations, the key findings are consistent between observations and the two model configurations with 1/4° and 1/12° resolution, respectively (Figures 8 and 9).

Relative to the respective model environment all features considered in this study (i.e., importance of strong eddies, size of eddies, mean background velocity, major eddy pathways) are well reproduced in both the 1/4° and the 1/12° simulation. But we also find striking differences between the models and the observations. Most importantly, there are fewer eddies detected in both model simulations compared to the observations (56% of the observed eddies in ANHA4 and 72% in ANHA4-SPG12). The eddy-permitting simulations show promising results for quantifying eddies in the North Atlantic relative to the respective model environment. However, our results suggest that a higher resolution than 1/12° is needed in order to fully reproduce the observed amount of eddies. Despite the different resolutions and the different numbers of eddies, the radii of the detected eddies are remarkably similar. So it is not simply the case that smaller eddies exist in the observations that are not reproduced in the models. There are overall fewer eddies in the models than in the observations, but the eddies that are formed in the models on average still show similar properties as the eddies in the observations. Therefore, even though we did not study the processes leading to the actual formation of eddies in this paper, it is likely that some of these processes (e.g., baroclinic instabilities) are not resolved in the models.

Strong eddies occur most often in the Newfoundland Basin, where they account for about one third of the temperature flux by eddies. The number of both regular and strong eddies in the region and their respective direction of translation are clearly connected to the position and strength of the background velocity field. *Dengler et al*. [2004] found that the Deep Western Boundary Current (DWBC) in the South Atlantic breaks up into eddies around 8°S, while for a weak DWBC a stable, laminar flow seems possible. We observe a similar behavior in the ANHA4 simulation where a weak NAC and WBC coincide with lower numbers of eddies compared to the observations and ANHA4-SPG12, where the background flow is stronger (Figures 7 and 8). The resulting temperature fluxes on the other hand are linked mostly to the SST anomalies, and even though we find the strongest fluxes in the region with the highest velocities, the direction of the temperature flux does not necessarily correspond to the direction of the mean velocity field.

Even though we find the largest fluxes in either direction in the western boundary region (mean northward flux 76.0 GW m^{-1} and mean southward flux -76.9 GW m^{-1}), the mean flux in western basin (subsection II) is practically zero because the large northward flux (especially in the NAC region) is compensated by large southward fluxes in the NBR region around 40°W and in the WBC. This result is supported by *Mertens et al*. [2014] who found that the largest part of the NAC recirculates locally in the Newfoundland Basin and about half of the WBC recirculates into the NAC. The eddies from the present study, first detected in the region between WBC and NAC (Figure 3c), provide a means for the local exchange between the boundary and the interior of the North Atlantic described by *Dutkiewicz et al*. [2001], *Bower et al*. [2009], and *Kieke et al*. [2009]. The eastern basin shows so few eddies crossing 47°N, because here the NAC runs mainly in a zonal direction northward of the section.

Several other studies have used satellite altimetry observations and automated eddy detection schemes to analyze mesoscale variability in the ocean. For example, *Chelton et al*. [2011] applied a SSH-based detection algorithm to 16 years of global AVISO altimetry data (October 1992 to December 2008) with 1/4° horizontal resolution (interpolated from 1/3°) and a 7 day temporal resolution. *Dong* [2012] used the same algorithm as we use in this study, but they applied it to a global set of geostrophic velocities from AVISO altimetry from January 1993 to December 2010 with 1/3° horizontal resolution and a 7 day temporal sampling. Despite the differences in method, temporal and spatial resolution and the different length of the time series, the spatial distributions of detected eddies in the subpolar North Atlantic by *Chelton et al*. [2011] and *Dong* [2012] agree well with the distribution of eddies found in this study.

The comparison of the distribution of detected eddies with the mean EKE in the region has shown that the two do not necessarily coincide (Figure 3). This is supported by *Rhein et al*. [2011] who found in a model that the strongest variability in the western basin is caused by meandering of the front between NAC and WBC rather than by actual eddies.

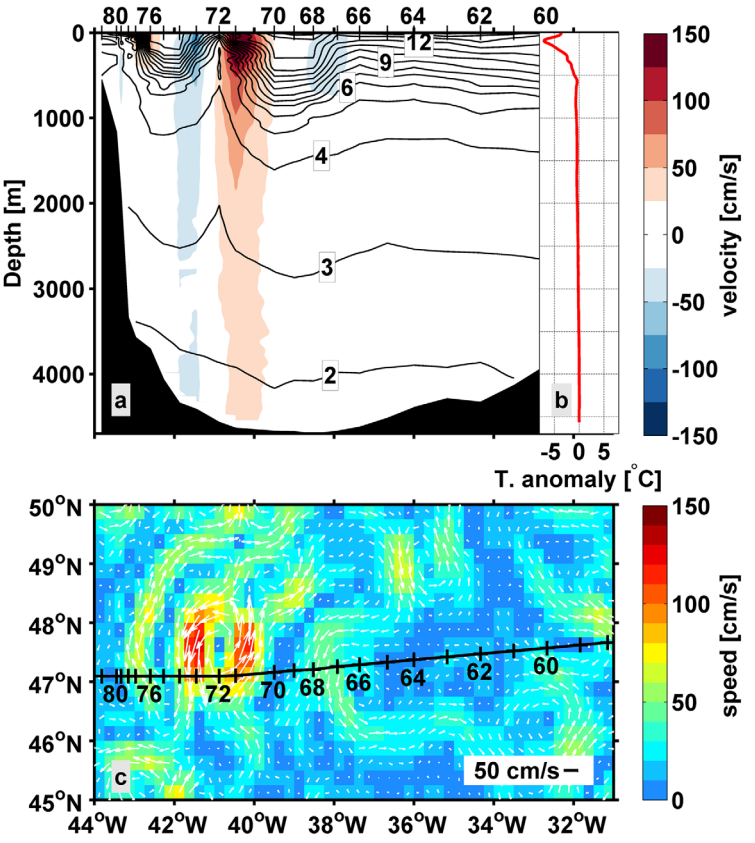

Figure 10. (a) Meridional velocities from LADCP measurements overlayed with potential temperatures from CTD measurements along 47°N. Measurements were carried out during RV Maria S. Merian cruise MSM43 between 11 June and 18 June 2015. Figure 10b shows the anomaly of the potential temperature inside the eddy (profile 72) with respect to the outside (average of profiles 71 and 73). Figure 10c shows a snapshot of the speed and the velocity vectors from near-real time AVISO geostrophic velocities on 16 June 2015 (day of profile 72 inside the eddy). The black line indicates the cruise track of the ship. The positions of the individual stations are marked at the top of Figure 10a and along the cruise track in Figure 10c.

Rossby [1996] has already described how the mean pathway of the NAC closely follows the bathymetry of the Newfoundland Basin, forms relatively stable meanders with cyclonic features located on the western side of the NAC and anticyclonic features on the eastern side. This admittedly schematic pathway of the NAC is reflected in the distribution of eddies along the Grand Banks. The cyclonic features on the western side of the NAC in turn coincide with the strong cyclonic eddies found in the present study. These features trap anomalously cold water from the WBC that is then carried back northward with the NAC, crossing 47°N in a narrow band around 40°W.

The open question still remaining is: How much of the total meridional heat flux at 47°N (about 0.6 PW [e.g., *Ganachaud and Wunsch*, 2000; *Rhein et al.*, 2011]) is achieved by eddies? With the current study we are not able to answer this question and can only assess the relative contribution of different types of eddies for the temperature flux by eddies. For a more complete understanding of the full heat flux by eddies, we need data from the deep ocean to infer the vertical structure of the eddy.

During RV Maria S. Merian cruise MSM43 in June 2015 a northward moving cold-core cyclonic eddy crossing 47°N was observed using LADCP and temperature measurements from Conductivity Temperature Depth (CTD) casts (Figure 10a). The eddy is also clearly visible in the near-real time AVISO geostrophic velocity field available for the same time (Figure 10b). The cruise track cuts through the southern part of the eddy, with CTD profile 72 located close to the center of the eddy and profiles 71 and 73 located in the eddy boundary where the rotational velocities are highest (>1 m s^{-1}). The regions of the highest velocities at the eastern and western eddy boundaries correspond to the strongest temperature gradients (Figure 10a). We find a surface temperature anomaly of more than -3.5°C when comparing the temperatures of profile 72 inside the eddy to the surrounding profiles 71 and 73. The maximum anomaly of almost -7°C is found at a depth of around 100 m. Below the depth of 500–600 m the temperature anomaly is much smaller than at the surface (Figure 10b), but the isotherms located at greater depth are still lifted by around 500 m. The observed surface temperature anomaly from CTD measurements fits well into the range of SST anomalies of strong eddies detected in the satellite observations. Even though the eddy described here is only one example of an in situ observed eddy, it shows the effect of strong cyclones in the NAC region and gives an idea about the vertical structure of eddies in the Newfoundland Basin that shall be further exploited.

Other studies [e.g., *Dong et al.*, 2014; *Zhang et al.*, 2013, 2014] have shown first attempts of combining detected eddies with observed temperature and salinity profiles from Argo floats. While this method shows

potential for extending the two dimensional surface fluxes in this study to full volume fluxes with a vertical component, presently available Argo observations in the North Atlantic are still too scarce to directly combine each detected eddy with a respective temperature or salinity profile. A promising method to infer the vertical structure of eddies from their respective SLA signature could be the Gravest Empirical Mode (GEM) technique [e.g., *Meinen and Watts*, 2000]. The GEM technique exploits the relationship between T/S profiles from Argo observations and dynamic height in order to parameterize temperature and salinity data as a function of dynamic height from the satellite altimetry [*Stendardo et al.*, 2016]. This method in combination with three-dimensional detection of eddies in high-resolution models could prove to be beneficial for understanding the connection between eddy surface signals and the corresponding vertical structure and will be investigated in a separate study. The aim is then to assess how much heat flux is achieved by actual eddies compared to the total heat flux at a given latitude and the so-called eddy-component of the heat flux calculated as $\overline{u'T'}$. The analysis can also be transferred to regions where observational data are scarce.

Acknowledgments

This study was supported by the Deutsche Forschungsgemeinschaft (DFG) through the International Research Training Group "Processes and impacts of climate change in the North Atlantic Ocean and the Canadian Arctic" (IRTG 1904 ArcTrain, VM) and by the Cluster of Excellence "The Oceans in the Earth System MARUM," subproject OC1 (DK), funded by the DFG. Support for the cruises came from the Co-Operative Project "RACE - Regional Atlantic Circulation and Global Change," grant 03F0651C, and Co-Operative Project "Nordatlantik," grants 03F0443C and 03F0605, all funded by the German Federal Ministry or Education and Research (BMBF), as well as the DFG through the Senate Commission on Oceanography. P.G.M. and C.P. gratefully acknowledge the financial and logistic support of grants from the Natural Sciences and Engineering Research Council (NSERC) of Canada. These include a Discovery Grant (rgpin 227438-09), Climate Change and Atmospheric Research Grant (VITALS - RGPCC 433898) and an International Create (ArcTrain - 432295). Observational data will be submitted to the PANGAEA database and made available to anyone upon request. NOAA Optimum Interpolation (Reynolds) Sea Surface Temperatures (https://www.ncdc.noaa.gov/oisst) have been obtained in netCDF file format by the Integrated Climate Data Center (ICDC, http://icdc.cen.uni-hamburg.de), University of Hamburg, Hamburg, Germany. The altimeter products were produced by Ssalto/Duacs and distributed by AVISO, with support from Cnes (http://www.aviso.altimetry.fr/duacs/). This research was enabled in part by support provided by WestGrid (www.westgrid.ca) and Compute Canada (www.computecanada.ca). We thank the three anonymous reviewers for their valuable comments that helped to improve this work. We further thank Francesco Nencioli (Plymouth, UK) for his helpful advice on using the eddy detection algorithm and Xianmin Hu (University of Alberta, Edmonton, Canada) for his help with the model simulations.

References

Abraham, E. R., and M. M. Bowen (2002), Chaotic stirring by a mesoscale surface-ocean flow, *Chaos*, *12*(2), 373–381, doi:10.1063/1.1481615.

Amante, C., and B. W. Eakins (2009), ETOPO1 1 arc-minute global relief model: Procedures, data sources and analysis, NOAA Tech. Memo. NESDIS NGDC-24, Natl. Geophys. Data Cent., NOAA, Boulder, Colo., doi:10.7289/V5C8276M.

Barnier, B., et al. (2007), Eddy-permitting ocean circulation hindcasts of past decades, *CLIVAR Exch.*, *42*(12), 8–10.

Bower, A. S., and W.-J. von Appen (2008), Interannual variability in the pathways of the North Atlantic Current over the Mid-Atlantic Ridge and the impact of topography, *J. Phys. Oceanogr.*, *38*(1), 104–120, doi:10.1175/2007JPO3686.1.

Bower, A. S., M. S. Lozier, S. F. Gary, and C. W. Böning (2009), Interior pathways of the North Atlantic meridional overturning circulation, *Nature*, *459*(7244), 243–247, doi:10.1038/nature07979.

Bower, A. S., S. Lozier, and S. Gary (2011), Export of Labrador Sea Water from the subpolar North Atlantic: A Lagrangian perspective, *Deep Sea Res., Part II*, *58*(17–18), 1798–1818, doi:10.1016/j.dsr2.2010.10.060.

Carr, M.-E., and H. T. Rossby (2001), Pathways of the North Atlantic Current from surface drifters and subsurface floats, *J. Geophys. Res.*, *106*(C3), 4405–4419, doi:10.1029/2000JC900106.

Chaigneau, A. S., A. Gizolme, and C. Grados (2008), Mesoscale eddies off Peru in altimeter records: Identification algorithms and eddy spatio-temporal patterns, *Prog. Oceanogr.*, *79*(2–4), 106–119, doi:10.1016/j.pocean.2008.10.013.

Chelton, D. B., R. A. DeSzoeke, M. G. Schlax, K. El Naggar, and N. Siwertz (1998), Geographical variability of the first baroclinic Rossby radius of deformation, *J. Phys. Oceanogr.*, *28*(3), 433–460, doi:10.1175/1520-0485(1998)028 < 0433:GVOTFB>2.0.CO;2.

Chelton, D. B., M. G. Schlax, R. M. Samelson, and R. A. de Szoeke (2007), Global observations of large oceanic eddies, *Geophys. Res. Lett.*, *34*, L15606, doi:10.1029/2007GL030812.

Chelton, D. B., M. G. Schlax, and R. M. Samelson (2011), Global observations of nonlinear mesoscale eddies, *Prog. Oceanogr.*, *91*(2), 167–216, doi:10.1016/j.pocean.2011.01.002.

Dai, A., T. Qian, K. E. Trenberth, and J. D. Milliman (2009), Changes in continental freshwater discharge from 1948 to 2004, *J. Clim.*, *22*(10), 2773–2792, doi:10.1175/2008JCLI2592.1.

Debreu, L., C. Vouland, and E. Blayo (2008), AGRIF: Adaptive grid refinement in Fortran, *Comput. Geosci.*, *34*(1), 8–13, doi:10.1016/j.cageo.2007.01.009.

Dengler, M., F. A. Schott, C. Eden, P. Brandt, J. Fischer, and R. J. Zantopp (2004), Break-up of the Atlantic deep western boundary current into eddies at 8°S, *Nature*, *432*(7020), 1018–1020, doi:10.1038/nature03134.

Doglioli, A. M., B. Blanke, S. Speich, and G. Lapeyre (2007), Tracking coherent structures in a regional ocean model with wavelet analysis: Application to Cape Basin eddies, *J. Geophys. Res.*, *112*, C05043, doi:10.1029/2006JC003952.

Dong, C. (2012), Global Eddy Data Set, IGPP, Los Angeles. [Available at http://people.atmos.ucla.edu/cdong/Global_Eddy_Data_SSHA/.]

Dong, C., J. C. McWilliams, Y. Liu, and D. Chen (2014), Global heat and salt transports by eddy movement, *Nat. Commun.*, *5*, Article 3294, doi:10.1038/ncomms4294.

Ducet, N., P. Y. Le Traon, and G. Reverdin (2000), Global high-resolution mapping of ocean circulation from TOPEX/Poseidon and ERS-1 and −2, *J. Geophys. Res.*, *105*(C8), 19,477–19,498, doi:10.1029/2000JC900063.

Dukhovskoy, D. S., P. G. Myers, G. Platov, M.-L. Timmermans, B. Curry, A. Proshutinsky, J. L. Bamber, E. Chassignet, X. Hu, C. M. Lee, and R. Somavilla (2016), Greenland freshwater pathways in the sub-Arctic Seas from model experiments with passive tracers, *J. Geophys. Res. Oceans*, *121*, 877–907, doi:10.1002/2015JC011290.

Dutkiewicz, S., L. Rothstein, and T. Rossby (2001), Pathways of cross-frontal exchange in the North Atlantic Current, *J. Geophys. Res.*, *106*(C11), 26,917–26,928, doi:10.1029/1999JC000089.

Egbert, G. D., and S. Y. Erofeeva (2002), Efficient inverse modeling of barotropic ocean tides, *J. Atmos. Oceanic Technol.*, *19*(2), 183–204, doi:10.1175/1520-0426(2002)019 < 0183:EIMOBO>2.0. CO;2.

Faghmous, J. H., I. Frenger, Y. Yao, R. Warmka, A. Lindell, and V. Kumar (2015), A daily global mesoscale ocean eddy dataset from satellite altimetry, *Sci. Data*, *2*, 150028, doi:10.1038/sdata.2015.28.

Ferry, N., L. Parent, G. Garric, B. Barnier, and N. C. Jourdain (2010), Mercator global Eddy permitting ocean reanalysis GLORYS1V1: Description and results, *Mercator Quart. Newsl.*, *34*, 15–27.

Fichefet, T., and M. A. Morales Maqueda (1997), Sensitivity of a global sea ice model to the treatment of ice thermodynamics and dynamics, *J. Geophys. Res.*, *102*(C6), 12,609–12,646, doi:10.1029/97JC00480.

Ganachaud, A., and C. Wunsch (2000), Improved estimates of global ocean circulation, heat transport and mixing from hydrographic data, *Nature*, *408*(6811), 453–457, doi:10.1038/35044048.

Hecht, M. W., and H. Hasumi (2008), *Ocean Modeling in an Eddying Regime, Geophys. Monogr. Ser.*, vol. 177, AGU, Washington, D. C., doi:10.1029/GM177.

Holdsworth, A. M., and P. G. Myers (2015), The influence of high-frequency atmospheric forcing on the circulation and deep convection of the Labrador Sea, *J. Clim.*, *28*(12), 4980–4996, doi:10.1175/JCLI-D-14-00564.1.

Hunke, E. C., and J. K. Dukowicz (1997), An elastic-viscous-plastic model for sea ice dynamics, *J. Phys. Oceanogr.*, *27*(9), 1849–1867, doi:10.1175/1520-0485(1997)027 < 1849:AEVPMF>2.0.CO;2.

Isern-Fontanet, J., E. García-Ladona, and J. Font (2003), Identification of marine eddies from altimetric maps, *J. Atmos. Oceanic Technol.*, *20*(5), 772–778, doi:10.1175/1520-0426(2003)20 < 772:IOMEFA>2.0.CO;2.

Kearns, E. J., and H. T. Rossby (1998), Historical position of the North Atlantic Current, *J. Geophys. Res.*, *103*(C8), 15,509–15,524, doi:10.1029/98JC00370.

Kieke, D., B. Klein, L. Stramma, M. Rhein, and K. P. Koltermann (2009), Variability and propagation of Labrador Sea Water in the southern subpolar North Atlantic, *Deep Sea Res., Part I*, *56*(10), 1656–1674, doi:10.1016/j.dsr.2009.05.010.

Köhler, J., M. Sena Martins, N. Serra, and D. Stammer (2015), Quality assessment of spaceborne sea surface salinity observations over the northern North Atlantic, *J. Geophys. Res. Oceans*, *120*, 94–112, doi:10.1002/2014JC010067.

Le Traon, P. Y., F. Nadal, and N. Ducet (1998), An improved mapping method of multisatellite altimeter data, *J. Atmos. Oceanic Technol.*, *15*(2), 522–534, doi:10.1175/1520-0426(1998) 015 < 0522:AIMMOM>2.0.CO;2.

Le Traon, P. Y., Y. Faugère, F. Hernandez, J. Dorandeu, F. Mertz, and M. Ablain (2003), Can we merge GEOSAT follow-on with TOPEX/Poseidon and ERS-2 for an improved description of the ocean circulation?, *J. Atmos. Oceanic Technol.*, *20*(6), 889–895, doi:10.1175/1520-0426(2003) 020 < 0889:CWMGFW>2.0.CO;2.

Liu, Y., C. Dong, Y. Guan, D. Chen, J. McWilliams, and F. Nencioli (2012), Eddy analysis in the subtropical zonal band of the North Pacific Ocean, *Deep Sea Res., Part I*, *68*, 54–67, doi:10.1016/j.dsr.2012.06.001.

Madec, G., and the NEMO team (2008), NEMO ocean engine, in *Note du Pôle Modélisation*, vol. 27, 357 pp., Inst. Pierre-Simon Laplace, France.

Mann, C. (1967), The termination of the Gulf Stream and the beginning of the North Atlantic Current, *Deep Sea Res. Oceanogr. Abstr.*, *14*(3), 337–359, doi:10.1016/0011-7471(67)90077-0.

Meinen, C. S., and D. R. Watts (2000), Vertical structure and transport on a transect across the North Atlantic Current near 42N: Time series and mean, *J. Geophys. Res.*, *105*(C9), 21,869–21,891, doi:10.1029/2000JC900097.

Mertens, C., M. Rhein, M. Walter, C. W. Böning, E. Behrens, D. Kieke, R. Steinfeldt, and U. Stöber (2014), Circulation and transports in the Newfoundland Basin, western subpolar North Atlantic, *J. Geophys. Res. Oceans*, *119*, 7772–7793, doi:10.1002/2014JC010019.

Nencioli, F., C. Dong, T. Dickey, L. Washburn, and J. C. McWilliams (2010), A vector geometry-based eddy detection algorithm and its application to a high-resolution numerical model product and high-frequency radar surface velocities in the Southern California Bight, *J. Atmos. Oceanic Technol.*, *27*(3), 564–579, doi:10.1175/2009JTECHO725.1.

Okubo, A. (1970), Horizontal dispersion of floatable particles in the vicinity of velocity singularities such as convergences, *Deep Sea Res. Oceanogr. Abstr.*, *17*(3), 445–454, doi:10.1016/0011-7471(70) 90059-8.

Pérez-Brunius, P., T. Rossby, and D. R. Watts (2004), Absolute transports of mass and temperature for the North Atlantic Current-subpolar front system, *J. Phys. Oceanogr.*, *34*(8), 1870–1883, doi:10.1175/1520-0485(2004)034 < 1870:ATOMAT>2.0.CO;2.

Reynolds, R. W., T. M. Smith, C. Liu, D. B. Chelton, K. S. Casey, and M. G. Schlax (2007), Daily high-resolution-blended analyses for sea surface temperature, *J. Clim.*, *20*(22), 5473–5496, doi:10.1175/2007JCLI1824.1.

Rhein, M., D. Kieke, S. Hüttl-Kabus, A. Roessler, C. Mertens, R. Meissner, B. Klein, C. W. Böning, and I. Yashayaev (2011), Deep water formation, the subpolar gyre, and the meridional overturning circulation in the subpolar North Atlantic, *Deep Sea Res., Part II*, *58*(17–18), 1819–1832, doi:10.1016/j.dsr2.2010.10.061.

Robinson, A. R. (1983), *Eddies in Marine Science*, Springer, Berlin Heidelberg, Germany.

Roessler, A., M. Rhein, D. Kieke, and C. Mertens (2015), Long-term observations of North Atlantic Current transport at the gateway between western and eastern Atlantic, *J. Geophys. Res. Oceans*, *120*, 4003–4027, doi:10.1002/2014JC010662.

Rossby, T. (1996), The North Atlantic Current and surrounding waters: At the crossroads, *Rev. Geophys.*, *34*(4), 463–481, doi:10.1029/96RG02214.

SSALTO/Duacs (2014), SSALTO/DUACS User Handbook: (M)*SLA* and (M)ADT Near-Real Time and Delayed Time Products, CLS-DOS-NT-06-034, Issue 4.4., Ramonville St Agne, France. [Available at http://www.aviso.altimetry.fr/fileadmin/documents/data/tools/hdbk_duacs.pdf]

Schott, F., L. Stramma, and J. Fischer (1999), Interaction of the North Atlantic Current with the deep Charlie Gibbs fracture zone throughflow, *Geophys. Res. Lett.*, *26*(3), 369–372, doi:10.1029/1998GL900223.

Smith, G. C., F. Roy, P. Mann, F. Dupont, B. Brasnett, J. F. Lemieux, S. Laroche, and S. Bélair (2014), A new atmospheric dataset for forcing ice-ocean models: Evaluation of reforecasts using the Canadian global deterministic prediction system, *Q. J. R. Meteorol. Soc.*, *140*(680), 881–894, doi:10.1002/qj.2194.

Stendardo, I., M. Rhein, and R. Hollmann (2016), A high resolution salinity time series 1993-2012 in the North Atlantic from Argo and Altimeter data, *J. Geophys. Res. Oceans*, *121*, 2523–2551, doi:10.1002/2015JC011439.

Visbeck, M. (2002), Deep velocity profiling using lowered acoustic doppler current profilers: Bottom track and inverse solutions, *J. Atmos. Oceanic Technol.*, *19*(5), 794–807, doi:10.1175/1520-0426(2002)019 < 0794:DVPULA>2.0.CO;2.

Waugh, D. W., and E. R. Abraham (2008), Stirring in the global surface ocean, *Geophys. Res. Lett.*, *35*, L20605, doi:10.1029/2008GL035526.

Weiss, J. (1991), The dynamics of enstrophy transfer in two-dimensional hydrodynamics, *Physica D*, *48*(2–3), 273–294, doi:10.1016/0167-2789(91)90088-Q.

Zhang, Z., Y. Zhang, W. Wang, and R. X. Huang (2013), Universal structure of mesoscale eddies in the ocean, *Geophys. Res. Lett.*, *40*, 3677–3681, doi:10.1002/grl.50736.

Zhang, Z., W. Wang, and B. Qiu (2014), Oceanic mass transport by mesoscale eddies, *Science*, *345*(6194), 322–324, doi:10.1126/science.1252418.